6

Linking ice and gas in the λ Orionis Barnard 35A cloud

G. Perotti[1], J. K. Jørgensen[1], H. J. Fraser[2], A.N. Suutarinen[2], L. E. Kristensen[1], W. R. M. Rocha[1], P. Bjerkeli[3], K. M. Pontoppidan[4]

[1] Niels Bohr Institute & Centre for Star and Planet Formation, University of Copenhagen, Øster Voldgade 5−7, 1350 Copenhagen K., Denmark
[2] School of Physical Sciences, The Open University, Walton Hall, Milton Keynes, MK7 6AA, United Kingdom
[3] Department of Space, Earth, and Environment, Chalmers University of Technology, Onsala Space Observatory, 439 92 Onsala, Sweden
[4] Space Telescope Science Institute, 3700 San Martin Drive, Baltimore, MD 21218, USA

Published in Astronomy & Astrophyics, vol. 650, article no. A168, Jun 2021

Abstract

Context. Dust grains play an important role in the synthesis of molecules in the interstellar medium, from the simplest species, such as H_2, to complex organic molecules. How some of these solid-state molecules are converted into gas-phase species is still a matter of debate.

Aims. Our aim is to directly compare ice and gas abundances of methanol (CH_3OH) and carbon monoxide (CO) obtained from near-infrared (2.5−5 μm) and millimetre (1.3 mm) observations and to investigate the relationship between ice, dust, and gas in low-mass protostellar envelopes..

Methods. We present Submillimeter Array (SMA) and Atacama Pathfinder EXperiment (APEX) observations of gas-phase CH_3OH ($J_K = 5_K - 4_K$), ^{13}CO, and $C^{18}O$ ($J = 2-1$) towards the multiple protostellar system IRAS 05417+0907, which is located in the B35A cloud, λ Orionis region. We use archival IRAM 30 m data and AKARI H_2O, CO, and CH_3OH ice observations towards the same target to

compare ice and gas abundances and directly calculate CH_3OH and CO gas-to-ice ratios.

Results. The CO isotopologue emissions are extended, whereas the CH_3OH emission is compact and traces the giant molecular outflow emanating from IRAS 05417+0907. A discrepancy between sub-millimetre dust emission and H_2O ice column density is found for B35A−4 and B35A−5, similar to what has previously been reported. B35A−2 and B35A−3 are located where the sub-millimetre dust emission peaks and show H_2O column densities lower than that of B35A−4.

Conclusions. The difference between the sub-millimetre continuum emission and the infrared H_2O ice observations suggests that the distributions of dust and H_2O ice differ around the young stellar objects in this dense cloud. The reason for this may be that the four sources are located in different environments resolved by the interferometric observations: B35A−2, B35A−3, and, in particular, B35A−5 are situated in a shocked region that is plausibly affected by sputtering and heating, which in turn impacts the sub-millimetre dust emission pattern, while B35A−4 is situated in a more quiescent part of the cloud. Gas and ice maps are essential for connecting small-scale variations in the ice composition with the large-scale astrophysical phenomena probed by gas observations.

6.1 INTRODUCTION

The interaction between dust, ice, and gas is ubiquitous in star-forming regions, and it is essential for the synthesis of interstellar molecules, the main ingredients for the origin of life on Earth. In recent decades, the number of detected molecules in the interstellar medium (ISM) increased considerably (McGuire, 2018) and with it the awareness of an interplay between solid and gaseous molecules in star-forming regions (Herbst and van Dishoeck, 2009; Boogert *et al.*, 2015; Jørgensen *et al.*, 2020; Öberg and Bergin, 2021). Some of the questions that remain to be answered regard the link between the distribution of solids (dust, ices) and gaseous molecules in molecular clouds and what this tells us about the solid-gas intertwined chemistries (e.g. the thermal and non-thermal desorption mechanisms that release solid-state molecules into the gas phase and vice versa).

Desorption mechanisms are of the utmost importance for understanding some critical aspects of star and planet formation (van Dishoeck and Blake, 1998). Besides enhancing the chemical complexity in the gas phase (Cazaux *et al.*, 2003; Jørgensen *et al.*, 2016; Bergner *et al.*, 2017; Calcutt *et al.*, 2018; Manigand *et al.*, 2020; van Gelder *et al.*, 2020), the positions in protostellar disks at which they occur (i.e., snow lines) influence the formation and evolution of planets (Öberg *et al.*, 2011b; Eistrup *et al.*, 2016; van 't Hoff *et al.*, 2017; Grassi *et al.*, 2020). Simultaneously, desorption processes can also shape the composition of grain surfaces. This is a consequence of the fact that all desorption mechanisms are much more efficient for volatile species (CO, O_2, and N_2; Bisschop *et al.*, 2006; Noble *et al.*, 2012; Cazaux *et al.*, 2017) than for less volatile species (H_2O and CH_3OH; Fraser *et al.*, 2001; Bertin

et al., 2016; Cruz-Diaz *et al.*, 2016; Martín-Doménech *et al.*, 2016). Since thermal desorption mechanisms alone can often not account for the diversity of species observed in star-forming regions, a further question remains as to the extent that the prevailing physical conditions might impact ice loss, for example through photo-desorption, sputtering, and chemical- and shock-induced processes (e.g. Kristensen *et al.*, 2010; Vasyunin and Herbst, 2013; Dulieu *et al.*, 2013; Öberg, 2016; Dartois *et al.*, 2019). Obtaining key insights into the desorption mechanisms is crucial for studying the composition of ice mantles, and hence the production of complex organics, during the early phases of star formation.

The preferred observational approach to constrain solid-state chemistry consists of inferring abundances of solid-state molecules based on their observed gas-phase emissions (Bergin and Tafalla, 2007; Öberg *et al.*, 2009a; Whittet *et al.*, 2011). Although this method of indirectly deriving ice abundances from gas-phase observations is the most used to get insights into the ice composition, it relies on major assumptions, for instance on the formation pathways and the desorption efficiency of solid-state species.

One way to test these assumptions is to combine ice and gas observations (i.e., ice- and gas-mapping techniques) and thus compare ice abundances with gas abundances towards the same region (Noble *et al.*, 2017; Perotti *et al.*, 2020). The evident advantage of combining the two techniques is that it enables us to study the distribution of gas-phase and solid-state molecules concurrently on the same lines of sight, and hence to address how solid-state processes are affected by physical conditions probed by gas phase-mapping such as density, temperature and radiation field gradients, turbulence and dust heating. However, the number of regions where such combined maps are available is still limited.

In this chapter we explore the interplay between ice and gas in the bright-rimmed cloud Barnard 35 (B35A; also known as BRC18, SFO18 and L1594) located in the λ Orionis star-forming region (Sharpless, 1959; Lada and Black, 1976; Murdin and Penston, 1977; Mathieu, 2008; Hernández *et al.*, 2009; Bayo *et al.*, 2011; Barrado *et al.*, 2011; Kounkel *et al.*, 2018; Ansdell *et al.*, 2020) at a distance of 410 ± 20 pc (GAIA DR2; Zucker *et al.*, 2019; Zucker *et al.*, 2020). The λ Orionis region is characterized by a core of OB stars enclosed in a ring of dust and gas (Wade, 1957; Heiles and Habing, 1974; Maddalena and Morris, 1987; Zhang *et al.*, 1989; Lang *et al.*, 2000; Dolan and Mathieu, 2002; Sahan and Haffner, 2016). The OB stars formed approximately 5 Myr ago, whereas the ring formation is less certain, occurring between 1 and 6 Myr ago due to a supernova explosion (Dolan and Mathieu, 1999; Dolan and Mathieu, 2002; Kounkel, 2020). The presence of strong stellar winds from the massive stars and ionization fronts in the region has shaped and ionized the neighbouring ring of gas leading to the formation of dense molecular clouds (e.g., B35A, B30; Barrado *et al.*, 2018) and photodissociation regions (PDRs; Wolfire *et al.*, 1989; De Vries *et al.*, 2002; Lee *et al.*, 2005). For instance, the stellar wind from λ Orionis, the most massive star of the Collinder 69 cluster (an O8III star; Conti and Leep, 1974), hits the western side of B35A compressing the cloud and forming a PDR between the molecular cloud edge and the extended HII region S264 (De Vries *et al.*, 2002; Craigon, 2015).

Star formation is currently occurring in B35A: the multiple protostellar system IRAS 05417+0907 (i.e., B35A–3) lies within the western side of the cloud (Figure 6.1.1). IRAS 05417+0907 was long thought to be a single source but it is a cluster of at least four objects (B35A–2, B35A–3, B35A–4 and B35A–5), which were partially resolved by *Spitzer* IRAC observations as part of the *Spitzer* c2d Legacy survey[1] (Evans *et al.*, 2014; Table 6.2.1). B35A–3 (i.e., IRAS 05417+0907) is a Class I YSO and it is the primary of a close binary system (Connelley *et al.*, 2008); the classification of the other sources remains uncertain. B35A–3 is emanating a giant bipolar molecular outflow extending in the NE/SW direction relative to λ Orionis and terminating in the Herbig-Haro object HH 175 (Myers *et al.*, 1988; Qin and Wu, 2003; Craigon, 2015; Reipurth, 2000). A detailed multi-wavelength analysis and characterization of HH 175 and of the multiple protostellar system presented by Reipurth and Friberg (2021).

[1] https://irsa.ipac.caltech.edu/data/SPITZER/C2D/cores.html

The ice reservoir towards the YSOs in B35A has been extensively studied by Noble *et al.* (2013) and Noble *et al.* (2017) and Suutarinen (2015a). These works were based on near-infrared spectroscopic observations (2.5–5 μm) with the AKARI satellite. In Noble *et al.* (2013), H_2O, CO_2, and CO ice features were identified towards all four YSOs, whereas Suutarinen (2015a) performed a multi-component, multi-line fitting of all the ice features towards the same B35A sources identified by Noble *et al.* (2013) and Evans *et al.* (2014), and in a method similar to that employed by Perotti *et al.* (2020) were able to extract the H_2O, CO, and CH_3OH ice column densities concurrently from the spectral data. It is these ice column densities that are used for comparison in the remainder of this chapter.

In parallel, the morphology and kinematics of the gas in B35A has been investigated using single-dishes such as the *James Clerk Maxwell Telescope* (JCMT) and the *Institut de Radio Astronomie Millimétrique* (IRAM) 30 m telescope by Craigon (2015). The survey mapped ^{12}CO, ^{13}CO, and C^{18}O J=3–2 and J=2–1 over a 14.6′× 14.6′ region and confirmed the existence of a bright and dense rim along the western side of B35A, heated and compressed by the stellar wind of the nearby λ Orionis, and of a giant bipolar outflow emanating from the YSO region.

To investigate the interaction between the solid (ice) and gas phases in the region, ice maps of B35A were compared to gas-phase maps in Noble *et al.* (2017). From the combination of ice- and gas-mapping techniques, no clear correlation was found between gas or dust to ice towards B35A. The local scale variations traced by the ice-mapping were not immediately related to large scale astrophysical processes probed by the dust and gas observations.

In this chapter, we present interferometric Submillimeter Array (SMA) observations of the $J_K = 5_K - 4_K$ rotational band of CH_3OH at 241.791 GHz and of the J=2–1 rotational bands of two CO isotopologues (^{13}CO and C^{18}O) towards the multiple protostellar system IRAS 05417+0907 in B35A. The angular resolution of the interferometric observations allows us to study the distribution of the targeted species in greater spatial detail compared to existing single-dish observations. To also recover the large-scale emission, the SMA observations are combined with single-dish data, thus resolving the protostellar system members and, concurrently probing the surrounding

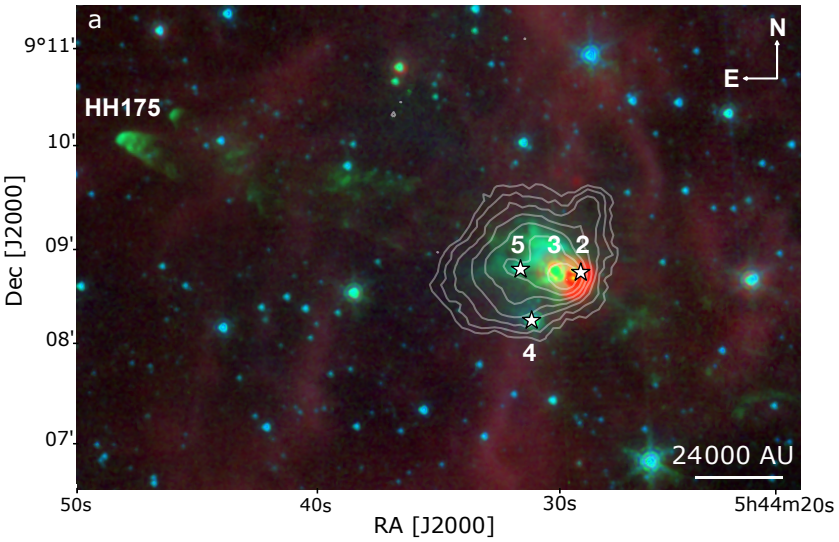

FIGURE 6.1.1: Three-color image of B35A overlaid with SCUBA−2 850 μm density flux in mJy beam^{-1} (Reipurth and Friberg, 2021; contours are in decreasing steps of 30% starting at 7.3 Jy beam^{-1}). The composite is made from *Spitzer* IRAC 3.6 μm (blue), 4.5 μm (green) and MIPS 24.0 μm (red) bands (Program ID: 139, PI: N. J. Evans II). The white stars mark the positions of the AKARI and *Spitzer* c2d identified B35A sources. Connelley *et al.* (2008) and Reipurth and Friberg (2021) show the B35A sources to be multiplet systems totalling 4 or 5 objects.

cloud. Furthermore, we produce ice and gas maps of a pivotal complex molecule, CH_3OH, and of one of its precursors, CO, to analyse the gas and ice interplay in the region. Lastly, we directly calculate gas-to-ice ratios of B35A to compare with ratios obtained for nearby star-forming regions.

The chapter is organised as follows. Section 6.2 describes the gas-phase observations and the archival data used to produce the gas and ice maps. Section 6.3 presents the results of the observations. Section 6.4 analyses the variations between the gas-phase and solid-state distributions of the different molecules. Section 6.5 discusses the observational results with a particular focus on the obtained gas-to-ice ratios. Finally, Section 6.6 summarises the main conclusions.

6.2 OBSERVATIONS AND ARCHIVAL DATA

6.2.1 *SMA and APEX observations*

The sample of sources was observed on September 19, 2018 with the *Submillimeter Array* (SMA; Ho *et al.*, 2004). The array was in its subcompact configuration with 7 operating antennas. The targeted region was covered by two overlapping pointings; the first pointing was centered on B35A−3 (i.e., IRAS 05417+0907) and the second was offset by one half primary beam to the south-east. Their exact coordinates are α_{J2000} = 05$^{\rm h}$44$^{\rm m}$30$^{\rm s}$.00, δ_{J2000} = +09°08′57″.3 and α_{J2000} = 05$^{\rm h}$44$^{\rm m}$30$^{\rm s}$.58, δ_{J2000} = +09°08′33″.8, respectively.

The SMA observations probed frequencies spanning from 214.3 to 245.6 GHz with a spectral resolution of 0.1 MHz (0.135 km s^{-1}). Among other species this frequency range covers the CH_3OH $J_K = 5_K - 4_K$ branch at 241.791 GHz, ^{13}CO $J = 2-1$ at 220.398 GHz and C^{18}O $J = 2-1$ at 219.560 GHz (Table 6.2.2). The observational setup consisted of a first long inte-

TABLE 6.2.1: Sample of sources.

Object[a]	RA [J2000]	DEC [J2000]	A_V [mag]
B35A–2	05:44:29.30	+09:08:57.0	52.7[b]
B35A–3	05:44:30.00	+09:08:57.3	54.9 ± 0.2[c]
B35A–4	05:44:30.85	+09:08:26.0	49.6 ± 2.3[c]
B35A–5	05:44:31.64	+09:08:57.8	19.5 ± 1.5[c]

Notes. [a] The objects are numbered according to the ID used in Noble *et al.* (2013). In Noble *et al.* (2017), objects 2, 3, 4, 5 are numbered 11, 1, 6 and 12, respectively. [b] For a detailed description of the A_V determination for B35A–2 see Section 6.3.3 and Appendix 6.B. [c] From the *Spitzer* c2d catalog[4].

TABLE 6.2.2: Spectral data of the detected molecular transitions.

Transition	Frequency[a] [GHz]	$A^a_{\rm ul}$ [s^{-1}]	$g^a_{\rm u}$	$E^a_{\rm u}$ [K]	$n^b_{\rm cr}$ [cm^{-3}]
$C^{18}O$ $J = 2 - 1$	219.560	6.01×10^{-7}	5	15.9	9.3×10^3
^{13}CO $J = 2 - 1$	220.398	6.04×10^{-7}	5	15.9	9.4×10^3
CH_3OH $J = 5_0 - 4_0$ E^+	241.700	6.04×10^{-5}	11	47.9	5.5×10^5
CH_3OH $J = 5_1 - 4_1$ E^-	241.767	5.81×10^{-5}	11	40.4	4.8×10^5
CH_3OH $J = 5_0 - 4_0$ A^+	241.791	6.05×10^{-5}	11	34.8	5.0×10^5
CH_3OH $J = 5_1 - 4_1$ E^+	241.879	5.96×10^{-5}	11	55.9	4.9×10^5
CH_3OH $J = 5_2 - 4_2$ E^-	241.904	5.09×10^{-5}	11	60.7	4.2×10^5

Notes. [a] From the Cologne Database for Molecular Spectroscopy (CDMS; Müller *et al.*, 2001) and the Jet Propulsion Laboratory catalog (Pickett *et al.*, 1998). [b] Calculated using a collisional temperature of 20 K and collisional rates from the Leiden Atomic and Molecular Database (LAMDA; Schöier *et al.*, 2005). The references for the collisional rates are Yang *et al.* (2010) for the CO isotopologues and Rabli and Flower (2010) for CH_3OH.

gration on the bandpass calibrator, the strong quasar 3c84, followed by alternated integrations on the source and on the gain calibrator, the quasar J0510+180. The absolute flux scale was obtained through observations of Uranus. The SMA data set was both calibrated and imaged using CASA[2] (McMullin *et al.*, 2007). At these frequencies, the typical SMA beam-sizes were $7\farcs3 \times 2\farcs4$ with a position angle of -32.2° for CH_3OH, and $7\farcs9 \times 2\farcs6$ with a position angle of -31.2° for ^{13}CO and $C^{18}O$.

[2] http://casa.nrao.edu/

To trace the more extended structures in the region, the SMA data were complemented by maps obtained using the *Atacama Pathfinder EXperiment* (APEX; Güsten *et al.*, 2006) on August 20–22, 2018. The single-dish observations covered frequencies between 236–243.8 GHz, matching the SMA 240 GHz receiver upper side band. The spectral resolution of the APEX observations was 0.061 MHz (0.076 km s^{-1}). The APEX map size was $100'' \times 125''$ and it extended over both SMA primary beams. The coordinates of the APEX pointing are $\alpha_{J2000} = 05^h44^m30^s.00$, $\delta_{J2000} = +09°08'57\farcs3$. The APEX beam size was $27\farcs4$ for the CH_3OH $J_K = 5_K - 4_K$ lines emission. The APEX

data set was reduced using the GILDAS package CLASS[3]. At a later stage, the reduced APEX data cube was imported to CASA and combined with the interferometric data using the feathering technique. A description of the combination procedure is given in Appendix 6.A.1.

[3] http://www.iram.fr/IRAMFR/GILDAS

6.2.2 *JCMT/SCUBA-2, Spitzer IRAC, 2MASS, IRAM 30 m and AKARI data*

Ancillary data to the SMA and APEX observations were adopted in this study. To construct H_2 column density maps of B35A, we used submillimeter continuum maps at 850 μm obtained with the SCUBA−2 camera at the *James Clerk Maxwell Telescope* (JCMT) by Reipurth and Friberg (2021), visual extinction values from the *Spitzer* c2d catalog[4] and 2MASS and *Spitzer* IRAC photometric data (Skrutskie *et al.*, 2006; Evans *et al.*, 2014). *Institut de Radio Astronomie Millimétrique* (IRAM) 30 m telescope observations (Craigon, 2015) were used to trace the extended emission for ^{13}CO and C^{18}O $J = 2{-}1$. Finally, to produce gas-ice maps of B35A we made use of the ice column densities determined by Suutarinen (2015a), from *AKARI* satellite observations.

[4] https://irsa.ipac.caltech.edu/data/SPITZER/C2D/cores.html

6.3 RESULTS

This section lists the observational results, supplying a summary of the methods employed to determine CO and CH_3OH gas column densities (Section 6.3.1 and Appendix 6.A). Additionally, it presents the H_2O, CO and CH_3OH ice column densities (Section 6.3.2) and the two H_2 column density maps used in the calculation of the abundances of the ice and gas species (Sect. 6.3.3).

6.3.1 *Gas-phase species*

The spectral line data of the detected molecular transitions are listed in Table 6.2.2. Figures 6.3.1–6.3.3 display moment 0 maps of the ^{13}CO and C^{18}O J=2−1 lines and CH_3OH J=5_0-4_0 A$^+$ line, using SMA, IRAM 30 m and APEX data. Moment 0 maps of the CH_3OH J=$5_0 - 4_0$ A$^+$ line are presented in this section as this transition is the brightest of the CH_3OH J=$5_K - 4_K$ branch at 241.791 GHz. The maps show that the SMA observations filter out spatially extended emission related to the B35A cloud. The SMA data only recover ≈10% of the extended emission detected in the single-dish data. Thus, consequently we need to combine the interferometric data with the single-dish maps in order not to underestimate the column densities severely.

Panels (a) of Figures 6.3.1–6.3.2 show that the interferometric emission is predominantly compact and the peak intensity is seen, for both CO isotopologues, at the location of B35A−2. The emission observed in the IRAM 30 m data sets (panels (b) of Figures 6.3.1–6.3.2) is extended and mostly concentrated around B35A−2, B35A−3 and B35A−5. In the combined SMA + IRAM 30 m maps (panels (c) of Fig. 6.3.1–6.3.2) the peak emission is also located in the region where B35A−2, B35A−3 and B35A−5 are present.

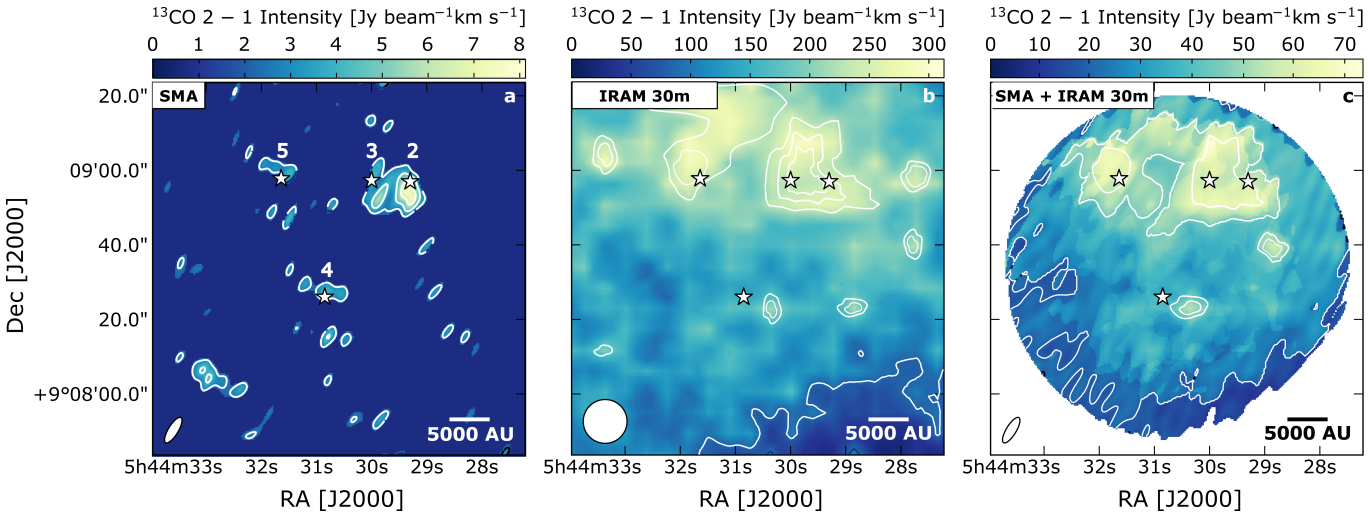

FIGURE 6.3.1: Integrated intensity maps for ^{13}CO J=2–1 detected by the SMA (a), by the IRAM 30 m telescope (b), and in the combined interferometric SMA and single-dish IRAM 30 m data (c). All lines are integrated between 7 and 16 km s^{-1}. Contours are at 5σ, 10σ, 15σ, etc. ($\sigma_{\rm SMA}$= 0.42 Jy beam^{-1}km s^{-1}, $\sigma_{\rm IRAM\ 30\ m}$= 6 Jy beam^{-1}km s^{-1}, $\sigma_{\rm SMA+IRAM\ 30\ m}$= 1.03 Jy beam^{-1}km s^{-1}). In panel (c), the white area outlines the primary beam of the SMA observations. The synthesized beams are displayed in white in the bottom left corner of each panel. The white stars mark the position of the targeted B35A sources.

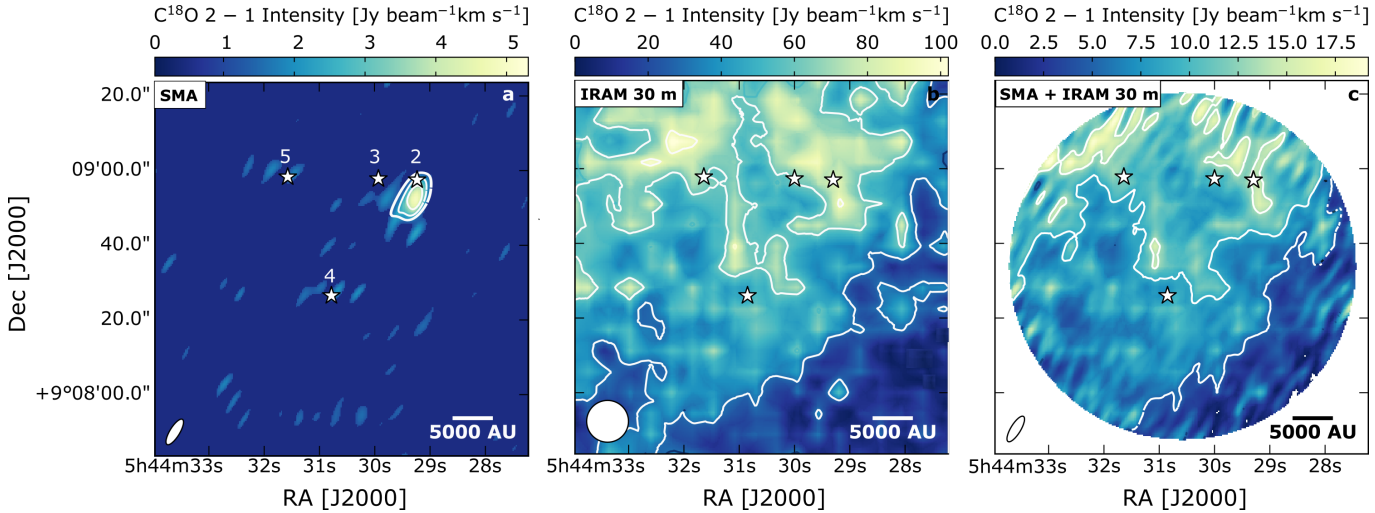

FIGURE 6.3.2: Integrated intensity maps for $C^{18}O$ J=2 – 1 detected by the SMA (a), by the IRAM 30 m telescope (b), and in the combined interferometric SMA and single-dish IRAM 30 m data (c). All lines are integrated between 10 and 15 km s^{-1}. Contours are at 5σ, 10σ, 15σ ($\sigma_{\rm SMA}$= 0.37 Jy beam^{-1}km s^{-1}, $\sigma_{\rm IRAM\ 30\ m}$= 5 Jy beam^{-1}km s^{-1}, $\sigma_{\rm SMA+IRAM\ 30\ m}$= 0.40 Jy beam^{-1}km s^{-1}). In panel (c), the white area outlines the primary beam of the SMA observations. The synthesized beams are displayed in white in the bottom left corner of each panel. The white stars mark the position of the targeted B35A sources.

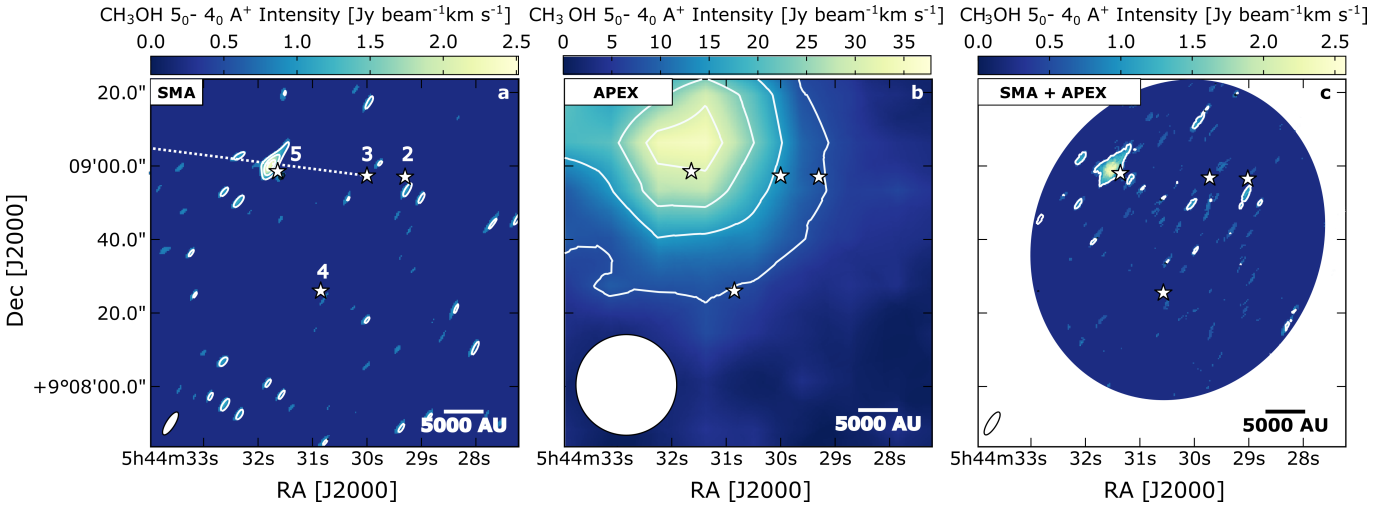

FIGURE 6.3.3: Integrated intensity maps for CH_3OH J=5_0 – 4_0 A^+ detected by the SMA (a), by the APEX telescope (b), and in the combined interferometric SMA and single-dish APEX data (c). All lines are integrated between 6 and 12.5 km s^{-1}. Contours start at 5σ (σ_{SMA}= 0.04 Jy $beam^{-1}$km s^{-1}, σ_{APEX}= 4 Jy $beam^{-1}$km s^{-1}, $\sigma_{SMA+APEX}$= 0.04 Jy $beam^{-1}$km s^{-1}) and follow a step of 5σ. In panel (c), the white area outlines the primary beam of the SMA observations. The synthesized beams are displayed in white in the bottom left corner of each panel. The white stars mark the position of the targeted B35A sources and the blue dotted line indicates the direction of the giant outflow terminating in HH 175.

TABLE 6.3.1: Total ice and gas column densities towards the B35A sources.

Object	$N^{\rm ice}_{\rm H_2O\ tot}$	$N^{\rm ice}_{\rm CO\ tot}$	$N^{\rm ice}_{\rm CH_3OH\ tot}$	$N^{\rm gas}_{\rm C^{18}O\ tot}$	$N^{\rm gas}_{\rm ^{12}CO\ tot}$	$N^{\rm gas}_{\rm CH_3OH\ tot}$	$^{\dagger}N^{\rm SCUBA-2}_{\rm H_2}$	$N^{A_V}_{\rm H_2}$
	$[10^{18}{\rm cm}^{-2}]$	$[10^{18}{\rm cm}^{-2}]$	$[10^{18}{\rm cm}^{-2}]$	$[10^{15}{\rm cm}^{-2}]$	$[10^{18}{\rm cm}^{-2}]$	$[10^{14}{\rm cm}^{-2}]$	$[10^{22}{\rm cm}^{-2}]$	$[10^{22}{\rm cm}^{-2}]$
B35A–2	2.96 ± 0.13	0.34 ± 0.03	0.26 ± 0.03	9.38 ± 1.92	5.22 ± 1.07	...	1.76 ± 0.09	7.22*
B35A–3	2.96 ± 0.12	0.32 ± 0.03	0.16 ± 0.03	7.02 ± 1.44	3.91 ± 0.80	...	1.69 ± 0.08	7.52 ± 0.02
B35A–4	3.35 ± 0.11	0.28 ± 0.06	0.10 ± 0.06	4.99 ± 1.03	2.78 ± 0.57	...	0.39 ± 0.02	6.79 ± 0.68
B35A–5	0.78 ± 0.12	< 0.18	< 0.18	7.11 ± 1.46	3.96 ± 0.81	1.91 ± 0.24	1.09 ± 0.05	2.66 ± 0.20

Notes. Columns 2–4 display the ice column densities from Suutarinen (2015a). Columns 5–7 list the gas column densities for $T_{\rm rot}$= 25 K. The errors are estimated based on the rms noise of the spectra and on the ~20% calibration uncertainty. Non-detections are indicated by ellipses. † $N^{\rm SCUBA-2}_{\rm H_2}$ is calculated using $T_{\rm dust}$= 25 K. The errors are calculated from the 5% flux calibration uncertainty and do not take the uncertainty on the $T_{\rm dust}$ into account. * The uncertainty on the A_V and consequently on the $N^{A_V}_{\rm H_2}$ for B35–2 is not estimated because this object is not detected in the J, H and K bands.

In contrast, the observed CH_3OH peak intensity is exclusively localized at the B35A−5 position in the SMA data (panel (a) of Fig. 6.3.3). B35A−5 lies along the eastern lobe of the giant bipolar molecular outflow emanated from IRAS 05417+0907 (i.e., B35A−3) and terminating at the location of the Herbig-Haro object HH 175 (Craigon, 2015). The CH_3OH emission is extended in the APEX data (panel (b) of Fig. 6.3.3) and hence not resolved at one particular source position. The emission in the SMA + APEX moment 0 map (panel (c) of Fig. 6.3.3) is compact and concentrated in one ridge in the proximity of B35A−5. The channel maps (Figures 6.A.3−6.A.5) and the spectra (Figure 6.A.1) extracted from the combined interferometric and single-dish data sets show predominantly blue-shifted components (Appendix 6.A.3). Blue- and red-shifted components are seen for the CO isotopologues, which were previously observed by De Vries *et al.* (2002), Craigon (2015) and Reipurth and Friberg (2021) and attributed to outflowing gas.

The ^{13}CO emission is optically thick towards the B35A sources, therefore the ^{13}CO column densities are underestimated towards the targeted region (Appendix 6.A.2). Consequently, the optically thin $C^{18}O$ emission is adopted to estimate the column density of ^{12}CO in B35A. First, $C^{18}O$ column densities towards the protostellar system members are obtained from the integrated line intensities of the combined SMA + IRAM 30 m maps (panels (c) of Figure 6.3.2), assuming optically thin emission and a kinetic temperature for the YSO region equal to 25 K (Craigon, 2015). The formalism adopted in the column density calculation is presented in Appendix 6.A.4, whereas the calculated $C^{18}O$ column densities and their uncertainties are listed in Table 6.3.1. The $C^{18}O$ column densities are converted to ^{12}CO column densities assuming a $^{16}O/^{18}O$ isotope ratio of 557 ± 30 (Wilson, 1999). The resulting ^{12}CO column densities (Table 6.3.1) are in good agreement with the values reported in Craigon (2015).

The CH_3OH column density towards B35A−5 is estimated from the integrated line intensities of the combined SMA + APEX maps for the five CH_3OH lines (Table 6.A.2), assuming optically thin CH_3OH emission, a kinetic temperature of 25 K (Craigon, 2015) and local thermodynamic equilibrium (LTE) conditions. The CH_3OH column density and its uncertainty is reported in Table 6.3.1. For all the gas-phase species, the uncertainty on the column densities is estimated based on the spectral rms noise and on the ∼20% calibration uncertainty.

6.3.2 *Ice column densities*

The ice column densities of H_2O, CO, and CH_3OH made use of in this chapter were originally derived by Suutarinen (2015a) from the AKARI (2.5−5 μm) NIR spectra of the targeted B35A sources. Suutarinen (2015a) adopted a non-heuristic approach, employing ice laboratory data and analytical functions to concurrently account for the contribution of a number of molecules to the observed ice band features. A detailed description of the AKARI observations is given in Noble *et al.* (2013) and the methodology adopted to derive the column densities of the major ice species can be found in Suutarinen (2015a).

The total ice column densities from Suutarinen (2015a) are listed in Table 6.3.1. Among the three molecules, H_2O ice is the most abundant in the ices of B35A, with column densities up to 3.35×10^{18} cm^{-2}, followed by CO and CH_3OH (Table 6.3.1). The column densities of the latter two molecules are comparatively one order of magnitude less abundant than H_2O ice. Upper limits are given for the CO and CH_3OH column densities towards B35A–5 because of difficulties in distinguishing the absorption features in the spectrum of this YSO (Noble *et al.*, 2013; Suutarinen, 2015a). A trend is observed for the CO and CH_3OH values: the column densities towards B35A–2 are the highest reported, followed by B35A–3, B35A–4 and B35A–5. The CO and CH_3OH ice column densities appear to follow the visual extinction with B35A–2 and B35A–3 being the most extincted sources and showing the highest CO and CH_3OH column densities (Tables 6.2.1 & 6.3.1). In this regard, it is important to recall that B35A–2 is not detected in the J, H, and K bands, making the determination of its visual extinction uncertain (Section 6.3.3 and Appendix 6.B).

6.3.3 H_2 column densities

An important factor to consider when combining ice- and gas-mapping techniques is that ice absorption and dust and gas emissions may probe different spatial scales (Noble *et al.*, 2017). As a matter of fact, the targeted sources may be embedded to different depths in the B35A cloud and consequently, the gas and ice observations may not be tracing the same columns of material. Therefore, the search for gas-ice correlations towards B35A has to be performed by comparing gas and ice abundances relative to H_2, following the approach adopted in Perotti *et al.* (2020).

To keep the gas and ice observations in their own reference frame, two H_2 column density maps are produced: one to derive gas abundances and one to determine ice abundances (Figure 6.3.4). For the gas observations, estimates of the H_2 column density are made using submillimeter continuum maps of B35A at 850μm (SCUBA–2; Reipurth and Friberg, 2021), under the assumption that the continuum emission is originated from optically thin thermal dust radiation (Kauffmann *et al.*, 2008). In this regime, the strength of the submillimeter radiation is dependent on the column density (N), the opacity (κ_ν) and the dust temperature (T). The adopted value for the opacity per unit dust+gas mass at 850 μm is 0.0182 cm^2 g^{-1} ("OH5 dust"; Ossenkopf and Henning, 1994). The temperature of B35A has been estimated by Morgan *et al.* (2008) and Craigon (2015). Both studies found two distinct regimes within the cloud: a cold region ($T_{\rm gas}$ = 10 – 20 K, $T_{\rm dust}$ = 18 K) in the shielded cloud interior to the east of the YSOs and a warm region ($T_{\rm gas}$ = 20 – 30 K) to the west of the YSOs. Since the region where the YSOs are located lies close to the warm cloud western edge, a $T_{\rm dust}$ = 25 K is adopted to estimate the H_2 column density map illustrated in Figure 6.3.4 (a) based on Craigon (2015) and Reipurth and Friberg (2021). The H_2 column density towards the B35A sources is reported in Table 6.3.1. The error on the H_2 column density was estimated according to the 5% flux calibration uncertainty (Dempsey *et al.*, 2013). Increasing the dust temperature to 30 K would lower the H_2 column density by 22% and consequently increase the

abundance of the gas-phase species by the same amount – while lowering the dust temperature to 18 K would increase the H_2 column density by 61% and consequently lowering the gas abundance likewise.

The above estimates assume an excitation temperature equal to 25 K for CO and CH_3OH. Increasing both the excitation temperature and the dust temperature to 30 K would result in gas abundances increasing by 24%. Conversely, lowering both temperatures to 18 K, would lower the abundances by 33%. A comprehensive description of the production of the H_2 column density map from SCUBA–2 measurements is given in Appendix C of Perotti *et al.* (2020).

The H_2 column density map calculated from the SCUBA–2 measurements supplies an accurate estimate of the total beam-averaged amount of gas towards B35A, and therefore provides a useful reference for the optically thin gas-phase tracers. However, the derived H_2 column density map can not directly be related to the AKARI data that supply (pencil-beam) measurements of the column densities towards the infrared sources that may or may not be embedded within the B35A cloud.

For the ice observations, the H_2 column density map is therefore obtained by performing a linear interpolation of the tabulated visual extinction (A_V) values for B35A taken from the *Spitzer* c2d catalog (see Appendix 6.B). Since no calculated A_V values are reported for B35A–2 and B35A–3, the A_V for B35A–3 is acquired by de-reddening the spectral energy distribution (SED) at the 2MASS J, H, K photometric points to fit a blackbody and using a second blackbody to model the infrared excess at longer wavelengths. A detailed description of the fitting procedure adopted for B35A–3 is given in Appendix 6.B. Following Evans *et al.* (2009) and Chapman *et al.* (2009), we adopt an extinction law for dense interstellar medium gas with $R_V = 5.5$ from Weingartner and Draine (2001) to calculate A_V. The visual extinction for B35A–2 could not be estimated through a similar procedure due to the lack of near-IR photometry data available for this object, thus the A_V for this source is obtained through the interpolation of the available visual extinction measurements for B35A. The final A_V values of the four sources are listed in Table 6.2.1. Finally, the visual extinction is converted to H_2 column density using the relation: $N_{H_2} = 1.37 \times 10^{21}$ cm^{-2} (A_V/mag) established for dense interstellar medium gas (Evans *et al.*, 2009). The H_2 column density calculated from the A_V map is shown in Figure 6.3.4 (b).

The H_2 column densities calculated from both methods are of the same order of magnitude, 10^{22} cm^{-2} (Table 6.3.1). The column densities differ by approximately a factor of 4 possibly due to variations in the exact column densities traced by SCUBA–2 and A_V measurements and assumptions on the dust temperature. In both H_2 column density maps (Fig. 6.3.4 a and b), it is seen that the four sources lie in the densest region of the cloud, confirming the results previously presented in Craigon (2015) and Reipurth and Friberg (2021). Although the two maps were calculated using two different methods, they reproduce the same trend: B35A–2 and B35A–3 are located where the H_2 column density peaks, whereas B35A–4 and B35A–5 are situated in less dense regions. However, in the H_2 column density map calculated from the visual extinction (Fig. 6.3.4 b), lower N_{H_2} values are reported for B35A–5 with respect to the other YSOs, whereas this is not the case in the H_2 column

density map calculated from the SCUBA−2 map (Fig. 6.3.4 a) where lower N_{H_2} values are observed for B35A−4. This difference can be explained by recalling that B35A−5 is the less extincted YSO ($A_V = 19.5$ mag) and it is located along the trajectory of the giant outflow launched by B35A−3. Consequently, the SCUBA−2 observations (14.6″ beam) are likely tracing the more extended structure of the dust emission in the region and not resolving the more compact emission towards each individual objects. It is worth observing that embedded protostars and Herbig-Haro objects can substantially affect the dust emission morphology (Chandler and Carlstrom, 1996), hence, the N_{H_2} enhancement seen in Figure 6.3.4 (a) likely reflects dust heating by the embedded protostars and by HH 175 resulting in an increase of the submillimeter continuum flux, rather than in an higher column density.

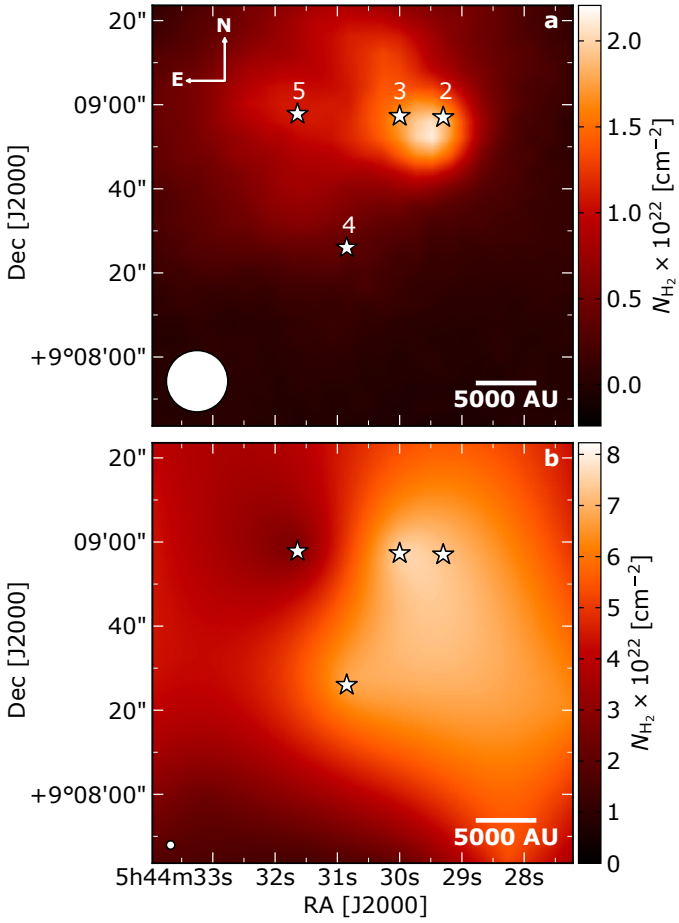

FIGURE 6.3.4: H_2 column density maps of B35A. *a*: N_{H_2} map calculated from SCUBA−2 dust emission at 850 μm (Reipurth and Friberg, 2021). *b*: N_{H_2} map calculated from the visual extinction. The synthesized beams are displayed in white in the bottom left corner of each panel. The white stars mark the positions of the targeted B35A sources.

6.4 ANALYSIS

6.4.1 *Gas-ice maps*

In Figure 6.4.1, the distributions of gas-phase ^{13}CO 2−1 (panel a) and C^{18}O 2−1 (panel b) emissions are compared to CO ice abundances. Both CO isotopologue emissions are concentrated at the B35A−2, B35A−3, B35A−5 source positions. The emission towards these three sources is of comparable intensity but it drops in the surroundings of B35A−4 and especially towards the southern edge of the cloud. The CO ice abundances with respect to H_2 are not characterized by large variations, instead, they are quite uniform and consistent within the uncertainties (Table 6.4.1). Only an upper limit could be determined for the CO ice column density towards B35A−5, due to the uncertainty in distinguishing the absorption feature at 3.53 μm in the spectrum of this object.

In Figure 6.4.1 (c), the distribution of gas-phase CH_3OH 5_0−4_0 A^+ emission is compared to CH_3OH ice abundances. As described in Section 6.3.1, the CH_3OH emission is concentrated solely in one ridge, located in proximity of the B35A−5 position. At this location only an upper limit on the CH_3OH ice abundance could be determined. The morphology of the CH_3OH emission suggests that while B35A−5 is situated in a shocked region, sitting along the trajectory of the giant outflow, B35A−4 lies in a more quiescent area, less influenced by high-velocity flows of matter. The CH_3OH ice abundances with respect to H_2 are characterized by slightly larger variations compared to CO ice (Table 6.4.1).

Finally, in Figure 6.4.1 (d), the distribution of gas-phase CH_3OH 5_0−4_0 A^+ emission is compared to H_2O ice abundances. The H_2O ice abundances are approximately one order of magnitude higher than the CO and CH_3OH ice abundances (Table 6.4.1). The lowest H_2O ice abundance is reported towards B35A−5 where the CH_3OH peak emission is observed. In contrast, the highest H_2O ice abundance is obtained towards B35A−4, where CH_3OH emission is not detected.

TABLE 6.4.1: Ice and gas abundances relative to H_2 towards the B35A sources.

Object	$X^{\rm ice}_{\rm H_2O}$	$X^{\rm ice}_{\rm CO}$	$X^{\rm ice}_{\rm CH_3OH}$	$X^{\rm gas}_{\rm ^{12}CO}$	$X^{\rm gas}_{\rm CH_3OH}$
	[10^{-5}]	[10^{-5}]	[10^{-5}]	[10^{-4}]	[10^{-8}]
B35A−2	4.10 ± 0.18	0.47 ± 0.04	0.36 ± 0.04	2.97 ± 0.63	...
B35A−3	3.99 ± 0.16	0.43 ± 0.04	0.21 ± 0.04	2.31 ± 0.49	...
B35A−4	4.93 ± 0.52	0.41 ± 0.50	0.15 ± 0.09	7.13 ± 1.50	...
B35A−5	2.93 ± 0.50	< 0.68	< 0.68	3.63 ± 0.76	1.75 ± 0.24

Notes. The column densities employed in the determination of the ice and gas abundances of H_2O, CO and CH_3OH are listed in Table 6.3.1. The abundances of the gaseous species are obtained using $N^{\rm SCUBA-2}_{\rm H_2}$, whereas the abundances of the ice species are relative to $N^{A_V}_{\rm H_2}$ (Table 6.3.1). Ellipses mark the non-detections of gas-phase CH_3OH.

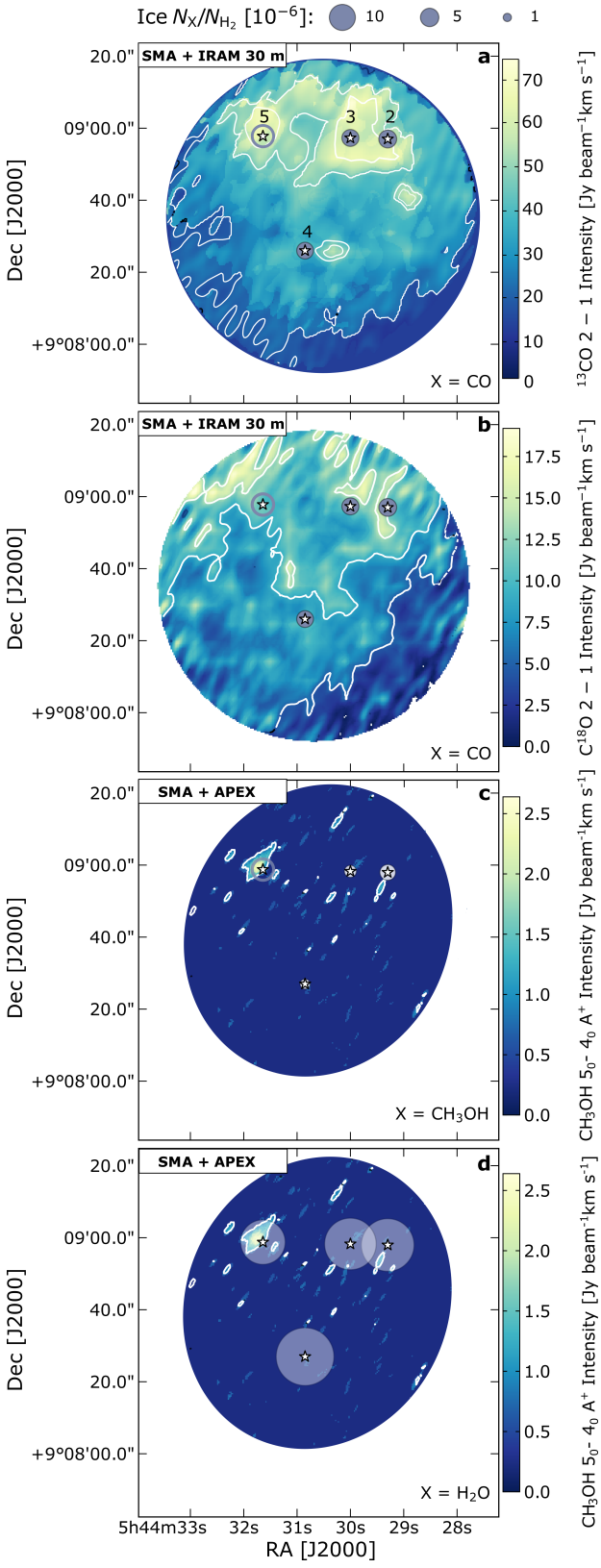

FIGURE 6.4.1: Gas-ice maps of B35A. Ice abundances are indicated as filled grey (panels a,b) or white circles (panels c and d), upper limits are displayed as empty circles. Contour levels are 5σ, 10σ, 15σ. *a:* CO ice abundances on gas ^{13}CO 2–1; *b:* CO ice abundances on gas C^{18}O 2–1 ; *c:* CH_3OH ice abundances on gas CH_3OH $5_0 - 4_0$ A^+. *d:* H_2O ice abundances on gas CH_3OH $5_0 - 4_0$ A^+. The white area outlines the primary beam of the SMA observations. The white stars mark the position of the targeted B35A sources.

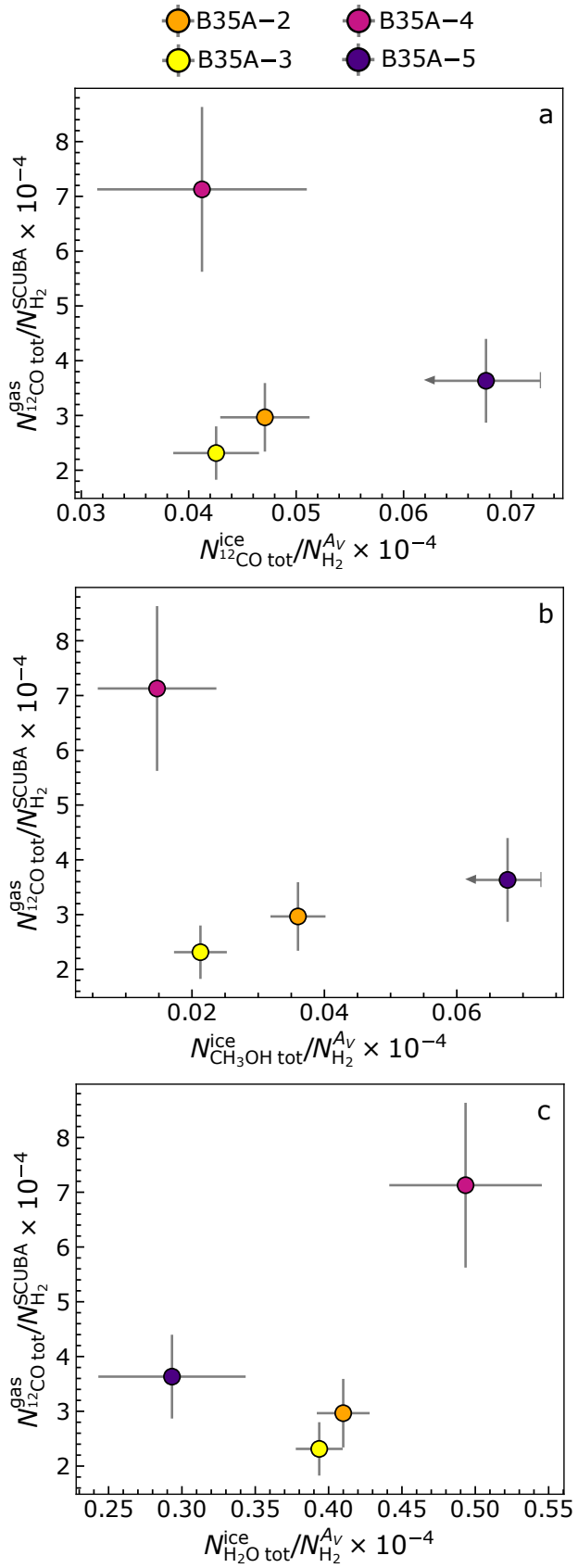

FIGURE 6.4.2: Gas and ice variations in B35A. The circles represent the targeted B35A sources. Panels (a) – (c) show the relation between CO, CH_3OH, and H_2O ice and CO gas abundances relative to H_2.

6.4.2 *Gas and ice variations*

In Figure 6.4.2, the search for gas-ice correlations towards B35A is addressed by analysing gas and ice abundances relative to H_2 (Table 6.4.1). The y-axes of all three panels display CO gas abundances, which are compared to abundances of CO ice (panel a), CH_3OH ice (panel b) and H_2O ice (panel c). To maintain gas and ice observations in their own reference frame, the CO gas abundances have been estimated using N_{H_2} calculated from SCUBA−2 850 μm maps, whereas the ice abundances have been calculated using N_{H_2} obtained from the visual extinction map (see Section 6.3.3 and Appendix 6.B). The formalism adopted to propagate the uncertainty from the column densities to the abundances is reported in Appendix 6.A.4.

It can be immediately noted that none of the ice species exhibits a predictable trend in ice abundance with gas abundance. Panels (a) and (b) show a similar behaviour since they are comparing molecules chemically linked - CO gas versus CO ice and CO gas vs CH_3OH ice being CO the precursor of CH_3OH. At the same time, panel (c) does not display the same relationships seen in the previous two panels. The latter observation is not surprising since there are no reasons for CO and H_2O to be directly linked from a purely chemical perspective.

In both panels (a) and (b) of Figure 6.4.2, B35A−4 displays the highest CO gas and the lowest CO and CH_3OH ice abundances. When the uncertainties are taken into account, the CO ice abundances towards B35A−2, B35A−3 and B35A−4 are alike (Table 6.4.1). For the CH_3OH ice abundances, B35A−3 and B35A−4 are consistent within the error bars, only towards B35A−2 a significant difference is found. Both CO and CH_3OH ice abundances towards B35A−5 are upper limits (Table 6.4.1). The similarity between CO and CH_3OH ice trends and the fact that the CH_3OH/CO ice ratios are > 0.3 indicates an efficient CH_3OH formation through CO hydrogenation (Watanabe and Kouchi, 2002) on the grain surfaces of B35A. The CO gas abundances towards B35A−2, B35A−3 and B35A−5 are in agreement within the uncertainties (Table 6.4.1).

In panels (c) some of the gas-ice variations differ with respect to panels (a) and (b): B35A−4 is characterized by the highest H_2O ice abundance, whereas B35A−5 shows the lowest H_2O ice abundance. This result corroborates the prediction that the ices of B35A−5 are the most depleted of volatile molecules among the B35A sources. The behaviours of B35A−2 and B35A−3 are similar if the uncertainties are considered (Table 6.4.1). The observed ice and gas variations between CO gas, CH_3OH gas and H_2O ice towards B35A−4 and B35A−5 favour a scenario in which H_2O ice is formed and predominantly resides on the ices of B35A−4, likely located in the most "quiescent" area of the targeted region, whereas in the proximity of a shocked region (B35A−5), H_2O ice mantles are partially desorbed. This result is discussed further in Sect. 6.5.1. Although the gas and ice variations analysed in this Section and in Sect. 6.4.1 are based on a small sample, they still highlight interesting trends in accordance to what we would expect from our knowledge of the physical structure of the targeted region.

6.4.3 *Comparison with previous gas-ice maps of B35A*

Noble *et al.* (2017) produced the first gas-ice maps of B35A. They compared AKARI ice abundances from Noble *et al.* (2013) with single-dish (JCMT/HARP and IRAM 30 m/HERA) gas-phase maps of $C^{18}O$ (Buckle *et al.*, 2009; Craigon, 2015; J=3−2 and 2−1), submillimeter continuum SCUBA maps at 850 μm, 450 μm/850 μm (Di Francesco *et al.*, 2008) and Herschel/SPIRE maps at 250 μm (Griffin *et al.*, 2010). The H_2 gas-phase map adopted to calculate ice abundances was determined from CO observations (Craigon, 2015).

Noble *et al.* (2013) and Noble *et al.* (2017) derived their ice column densities without considering the presence of CH_3OH, thus the H_2O ice column densities were routinely higher than those used here from Suutarinen, 2015a; Figure 6.4.3. Simultaneously, the CO ice column densities were calculated using different laboratory data (e.g., the CO-ice red component was fitted using a CO:H_2O (Fraser and van Dishoeck, 2004) laboratory spectrum as opposite to the CO:CH_3OH mixture (Cuppen *et al.*, 2011), resulting in higher CO-ice column density compared to Suutarinen (2015a).

The combination of gas, dust, and ice observations proposed in Noble *et al.* (2017) is characterised by a number of limitations which are taken into account in the presented work. The lower angular resolution of the adopted single-dish observations, the analysis of the chemical behaviours of simple molecules only (e.g., H_2O, CO, and CO_2) and the avoidance to consider that the ice and gas observations might probe different depths are some of them. The presented work overcomes these limitations by making use of higher angular resolution interferometric observations, studying the ice and gas variations of both simple (H_2O, CO) and complex molecules (CH_3OH) and lastly, by comparing ice and gas abundances derived using two different H_2 column density maps (to keep the ice and gas observations in their own reference frame).

From the analysis of the gas-ice maps, Noble *et al.* (2017) inferred that the dust in B35A is mainly localised around B35A−2 and B35A−3, in agreement with the higher ice column densities of H_2O and CO towards these two sources (Figure 6.4.3). However, they observed that the H_2O ice column densities are lower towards B35A−5 compared to B35A−4, even though the dust emission is higher towards B35A−5. The authors concluded that no clear trend is seen between ice, dust and gas in B35A and that more knowledge of the local-scale astrophysical environment is needed to disentangle the exact interplay between ice and gas in the region. The findings of Noble *et al.* (2017) are in agreement with the observational results and the gas-ice maps of B35A presented here (with the caveat that both CO ice abundances towards B35A−5 in Noble *et al.* (2017) and in this work are upper limits). However, the gas-ice maps produced in this study allow to explain that the lower H_2O ice abundance towards B35A−5 compared to B35A−4 is plausibly caused by the influence of shocks on the ice chemistry. CH_3OH is a tracer of energetic inputs in the form of outflows (Kristensen *et al.*, 2010; Suutarinen *et al.*, 2014), and it traces the trajectory of the bipolar outflow in B35A. As a result, lower H_2O ice abundances towards B35A−5 are likely the result of sputtering effects in the outflow shocks (e.g., Suutarinen *et al.*, 2014 and

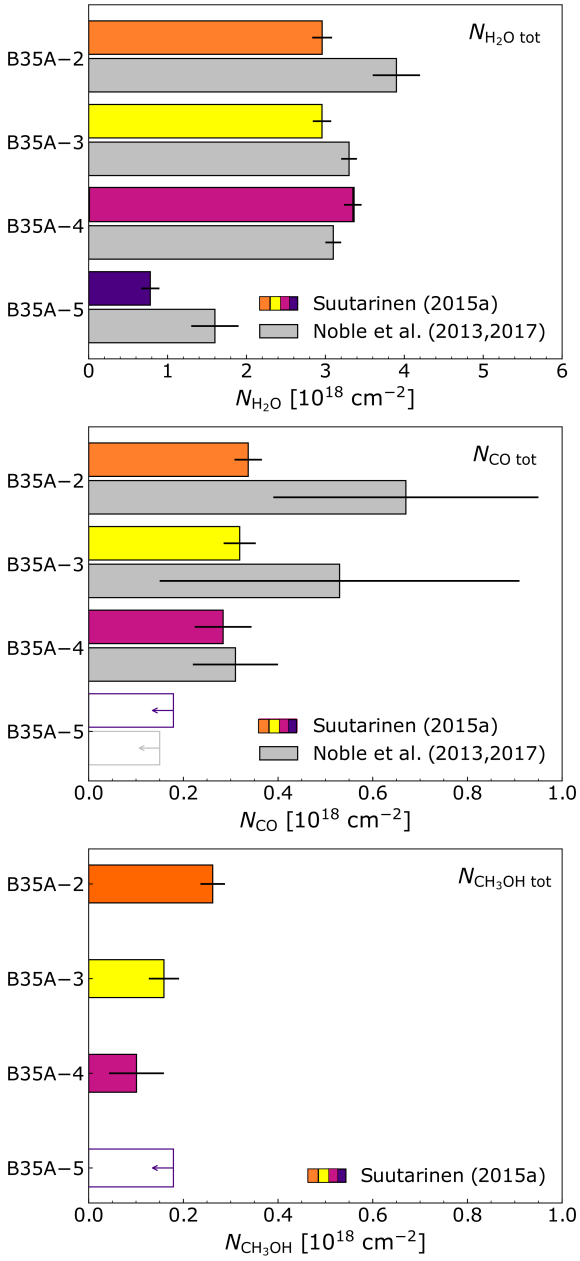

FIGURE 6.4.3: H_2O (top), CO (middle) and CH_3OH (bottom) total ice column densities obtained in Suutarinen (2015a) (the sources are colour-coded) compared to Noble *et al.* (2017) (light grey). The empty bars represent upper limits on the column densities.

references therein). Simultaneously, the fact that the submillimeter dust emission towards B35A–5 is high where the H_2O ice abundances are lower can also be explained by the presence of the outflow terminating in the HH object 175. In fact, UV radiation generated in the Herbig-Haro object itself may locally heat the dust, enhancing the sub-millimeter continuum flux of the region (Chandler and Carlstrom, 1996; Kristensen *et al.*, 2010; Figure 6.3.4 *a*).

6.5 DISCUSSION

The CH_3OH gas abundances in B35A (10^{-8}) are greater than what could be inferred by pure gas-phase synthesis (e.g., Garrod and Herbst, 2006). Hence, the observed CH_3OH gas must be produced on the grain surfaces and be desorbed afterwards. In the following, the preferred scenario for CH_3OH desorption in B35A is discussed. Additionally, the observational results presented in Sections 6.3.1–6.3.2 are employed to determine CH_3OH and CO gas-to-ice ratios (N_{gas}/N_{ice}) towards the multiple protostellar system in B35A. Finally, a comparison between the gas-to-ice ratios directly determined towards B35A and the gas-to-ice ratios of nearby star-forming regions is proposed.

6.5.1 *Sputtering of CH_3OH in B35A*

In Sections 6.3.1 and 6.4.1, it is seen that the CH_3OH emission is concentrated almost exclusively in one ridge, which coincides with the B35A–5 position. B35A–5 sits along the eastern lobe of a large collimated outflow emanated from the binary Class I IRAS 05417+0907 (i.e, B35A–3). The eastern lobe has a total extent of 0.6 pc and it terminates into the Herbig-Haro object HH 175 (Craigon, 2015). The total extent of the outflow is 1.65 pc (Reipurth and Friberg, 2021), which places HH 175 among the several dozens HH objects with parsec dimensions (Reipurth and Bally, 2001). Herbig-Haro objects are omnipresent in star-forming regions, but it is still not clear how exactly they are tied into the global star-formation process, e.g., how do they alter the morphology and kinematics of the gas in which they originate. These are highly energetic phenomena which are believed to form when high-velocity protostellar jets collide with the surrounding molecular cloud, inducing shocks. Such shocks compress and heat the gas, generating UV radiation (Neufeld and Dalgarno, 1989). The activity of Herbig-Haro objects can dramatically change the chemical composition of the gas in their vicinity, mutating the chemistry of the region during so-called sputtering processes (Neufeld and Dalgarno, 1989; Hollenbach and McKee, 1989).

Sputtering takes place in shocks when neutral species (e.g., H_2, H or He) collide with the surface of ice-covered dust grains with sufficient kinetic energy to expel ice species (e.g., CH_3OH, NH_3, H_2O) into the gas phase (Jørgensen *et al.*, 2004; Jiménez-Serra *et al.*, 2008; Kristensen *et al.*, 2010; Suutarinen *et al.*, 2014; Allen *et al.*, 2020). During a sputtering event, the ice molecules can desorb intact or be destroyed (e.g., via dissociative desorption) either due to the high kinetic energy or by reactions with H atoms (Blanksby and Ellison, 2003; Dartois *et al.*, 2019; Dartois *et al.*, 2020).

The fragments of dissociated molecules can then readily recombine in the gas-phase (Suutarinen *et al.*, 2014 and references therein).

The inferred dust temperatures in the B35A region (20–30 K) are remarkably lower than the CH_3OH sublimation temperature (~128 K; Penteado *et al.*, 2017), excluding thermal desorption as potential mechanism triggering the observed CH_3OH emission. This consideration, together with the observation of the CH_3OH emission along the HH 175 flow direction and the anticorrelation between CH_3OH emission and the lower H_2O ice abundances towards B35A–5 suggests that ice sputtering in shock waves is a viable mechanism to desorb ice molecules in B35A. Simultaneously, the absence of shocks towards B35A–4 likely explains the highest abundance of H_2O ice observed in this more quiescent region (Figure 6.4.1 d). Higher angular resolution observations of CH_3OH in the region are required to provide quantitative measurements of the amount of CH_3OH desorbed via sputtering compared to other non-thermal desorption mechanisms. Additional gas-phase observations of H_2O towards the B35A sources are needed to constrain further the processes linking H_2O ice and H_2O gas in this shocked region (e.g., sputtering of H_2O ice mantles versus direct H_2O gas-phase synthesis) and, in a broader context to contribute explaining the high abundances of H_2O observed in molecular outflows (Nisini *et al.*, 2010; Bjerkeli *et al.*, 2012; Bjerkeli *et al.*, 2016; Santangelo *et al.*, 2012; Vasta *et al.*, 2012; Dionatos *et al.*, 2013).

6.5.2 *Gas-to-ice ratios*

Figure 6.5.1 displays the CH_3OH (panel a) and CO (panel b) gas-to-ice ratios towards ten sources constituting the SVS 4 cluster located in the Serpens molecular cloud (Perotti *et al.*, 2020) and towards the B35A sources in the Orion molecular cloud. The shaded areas indicate the estimated ranges of gas-to-ice ratios towards both molecular clouds, providing complementary information of the gas-to-ice ratios of both regions compared to the value calculated towards each individual source.

Figure 6.5.1 (a) shows the CH_3OH gas-to-ice ratios ($N_{CH_3OH_{gas}}/N_{CH_3OH_{ice}}$) towards the SVS 4 sources and B35A–5. Only an upper limit for the CH_3OH gas-to-ice towards B35A–5 is obtained (i.e., 1.1×10^{-3}) due to the uncertainty on the CH_3OH ice column density determination towards this source (Suutarinen, 2015a). Therefore, only limited information is available on the CH_3OH chemistry in B35A. Figure 6.5.1 (a) also displays the averaged CH_3OH gas-to-ice ratio towards four low-mass embedded protostars located in nearby star-forming regions from Öberg *et al.* (2009a). A detailed comparison between the CH_3OH gas-to-ice ratios for the SVS 4 cluster members and the value estimated by Öberg *et al.* (2009a) is given in Perotti *et al.* (2020), and therefore not repeated here.

The observations of B35A address cold quiescent CH_3OH emission (J= 5_K–4_K transitions at 241.7 GHz and E_u from 34.8 to 60.7 K, see Table 6.2.2) and presumably quiescent gas not affected by outflow shocks and/or thermally desorbed in the vicinity of the protostar. The same applies to the observations presented in Öberg *et al.* (2009a); J= 2–1 transitions at 96.7 GHz and E_u in the range 14.4–35.4 K). However, B35A–5 and the SVS 4 sources

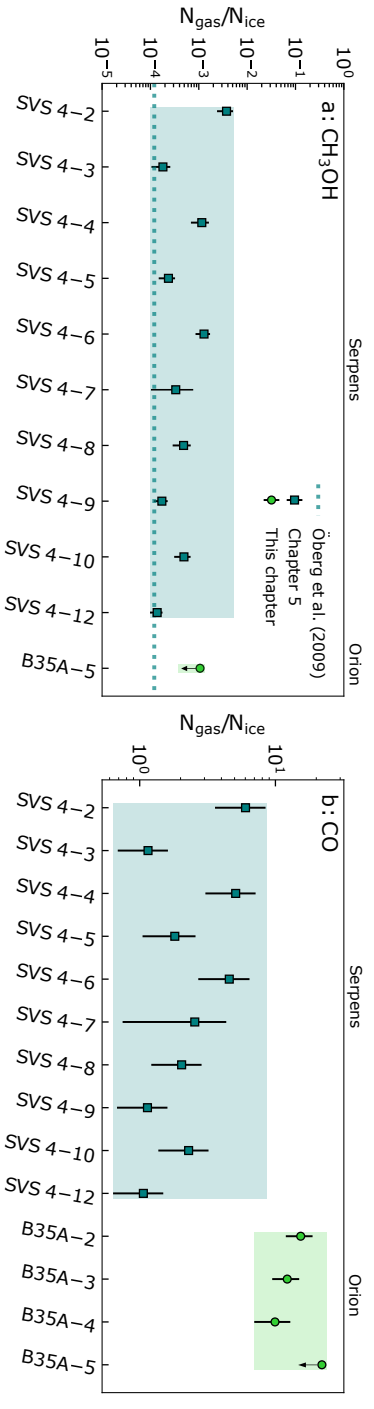

FIGURE 6.5.1: CH_3OH (panel a) and CO (panel b) gas-to-ice ratios (N_{gas}/N_{ice}) for the multiple protostellar system in Orion B35A and Serpens SVS 4. The dark green squares indicate the gas-to-ice ratios estimated in Chapter 5 for the Serpens SVS 4 cluster. The light green circles mark the ratios calculated in this chapter. The dotted light blue line in panel (a) represents the ratio estimated by Öberg *et al.* (2009a) towards Class 0/I objects. The shaded areas indicate the estimated ranges of the gas-to-ice ratios.

reporting the highest gas-to-ice ratios are likely affected to some extent by outflow shocks (i.e., B35A–5 by the giant outflow terminating in HH 175 and the SVS 4 sources by the outflow notoriously associated to SMM 4). This might justify the mismatch between Öberg *et al.* (2009a) value and the higher values of the gas-to-ice ratios. In the case of the B35A cloud, high-sensitivity infrared observations of B35A are required to constrain further this observation.

CO gas-to-ice ratios ($N_{CO_{gas}}/N_{CO_{ice}}$) towards the SVS 4 and B35A sources are illustrated in Figure 6.5.1 (b). As discussed previously in Perotti *et al.* (2020), the range of gas-to-ice ratios for SVS 4 extends between 1 and 6 and it is significantly higher than the predicted value (~4×10^{-2}; Cazaux *et al.*, 2016). This theoretical prediction is estimated from the three-phase astrochemical model by Cazaux *et al.* (2016) which includes thermal and non-thermal desorption processes of the species constituting the ice mantles. This comparison with the theoretical prediction has to be taken with care, since the physical model is not specifically tuned to reproduce the structures of the SVS 4 cluster or the B35A cloud. The estimated dust temperature towards the SVS 4 cluster is below 20 K (Kristensen *et al.*, 2010), indicating that CO is likely frozen out on the grain surfaces in this temperature range. We concluded from the high relative CO gas abundances that the gas-mapping is not tracing the densest regions of the SVS 4 cluster but an extended component that is not sensitive to the effect of freeze-out (Figure 8 of Perotti *et al.*, 2020).

High CO gas-to-ice ratios are also observed for B35A, but in this case they are mainly attributable to CO thermally desorbed in the region. The physical conditions of B35A and SVS 4 differ significantly, for example, the western side of B35A is highly influenced by the ionization-shock front driven by the λ Orionis OB stars and the dust temperature in the YSOs region of B35A has been estimated to be at least 25–30 K (Craigon, 2015; Morgan *et al.*, 2008). Therefore, at these temperatures, above the CO sublimation temperature (~20 K; Bisschop *et al.*, 2006; Collings *et al.*, 2004; Acharyya *et al.*, 2007), CO is efficiently thermally desorbed from the grain surfaces and it is expected to primarily reside in the gas-phase. According to this result, the observed CH_3OH ice might have formed at earlier stages, prior to the warm-up of the dust grains or alternatively, from CO molecules trapped in porous H_2O matrices, and therefore not sublimated at these temperatures. Additionally, higher abundances of CO might reflect an active CO gas-phase synthesis in the region. Follow-up observations of higher J transitions of CO isotopologues are required to provide a conclusive assessment.

6.6 CONCLUSIONS

Millimetric (SMA, APEX, IRAM 30 m) and infrared (AKARI) observations are used to investigate the relationships between ice, dust, and gas in the B35A cloud, associated with the λ Orionis region. Gas and ice maps are produced to compare the distribution of solid (H_2O, CO, and CH_3OH) and gaseous (^{13}CO, $C^{18}O$, and CH_3OH) molecules and to link the small-scale variations traced by ice observations with larger-scale astrophysical phenomena probed by gas observations. The main conclusions are:

- The CO isotopologues emission is extended in B35A, whereas the observed CH_3OH emission is compact and centred in the vicinity of B35A−5. B35A−5 sits along the trajectory of the outflow emanated from IRAS 05417+0907 (i.e., B35A−3), thus the observed gas-phase CH_3OH may be plausibly explained by sputtering of ice CH_3OH in the outflow shocks.
- The dust column density traced by the sub-millimetre emission is not directly related to the ice column inferred from the infrared observations. The sub-millimetre dust emission is stronger towards B35A−2, B35A−3, and B35A−5 compared to B35A−4; however, the H_2O ice column density is higher for B35A−4. This discrepancy is understood by taking into account the fact that B35A−2, B35A−3, and B35A−5 are situated in a shocked region that is affected by the presence of the Herbig-Haro object HH 175 – and thus likely influenced by sputtering and heating affecting the observed sub-millimetre dust emission pattern.
- None of the ice species shows a predictable trend in ice abundance with gas-phase abundance. This implies that inferring ice abundances from known gas-phase abundances and vice versa is inaccurate without an extensive knowledge of the physical environment of the targeted region.
- The high CO gas-to-ice ratios suggest that the CO molecules are efficiently thermally desorbed in B35A. This is supported by dust temperature estimates (25−30 K) towards the B35A sources above the CO sublimation temperature (~20 K).
- Simultaneously, the dust temperatures in the region are significantly lower than the CH_3OH sublimation temperature (128 K), excluding thermal desorption as the mechanism responsible for the observed CH_3OH emission.
- The combination of gas- and ice observations is essential to comprehend the relationships at the interface between solid and gas phases, and hence to link the small-scale variations detected in the ice observations with large-scale phenomena revealed by gas-phase observations.

The presented work is a preparatory study for future combined *James Webb Space Telescope* (JWST) and *Atacama Large Millimeter/submillimeter Array* (ALMA) observations, which will shed further light on the dependences of gas-to-ice ratios on the physical conditions of star-forming regions. In fact, future mid-infrared facilities, notably JWST, will considerably increase the number of regions for which ice maps are available. Such high-sensitivity ice maps can then be combined with ALMA observations to provide better constraints on the complex interplay between ice, dust, and gas during the earliest phases of star formation. The present study already shows that such gas-ice maps will be valuable given that they probe ice- and gas-phase chemistries to a greater extent than ice or gas maps alone.

ACKNOWLEDGEMENTS

The authors wish to thank Bo Reipurth for fruitful discussions on HH 175 and Alison Craigon, Zak Smith, Jennifer Noble for providing the reduced IRAM 30 m data. The authors also wish to acknowledge the anonymous

reviewer for the careful reading of the manuscript and the useful comments. This work is based on observations with the Submillimeter Array, Mauna Kea, Hawaii, program code: 2018A-S033, with the Atacama Pathfinder Experiment, Llano Chajnantor, Chile, program code: 0102.F-9304. The Submillimeter Array is a joint project between the Smithsonian Astrophysical Observatory and the Academia Sinica Institute of Astronomy and Astrophysics and is funded by the Smithsonian Institution and the Academia Sinica. The Atacama Pathfinder EXperiment (APEX) telescope is a collaboration between the Max Planck Institute for Radio Astronomy, the European Southern Observatory, and the Onsala Space Observatory. Swedish observations on APEX are supported through Swedish Research Council grant No 2017-00648. The study is also based on data from the IRAM Science Data Archive, obtained by H.J.Fraser with the IRAM 30 m telescope under project ID 088-07. Finally, this work is based on archival data from the AKARI satellite, a JAXA project with the participation of the European Space Agency (ESA). The group of JKJ acknowledges the financial support from the European Research Council (ERC) under the European Union's Horizon 2020 research and innovation programme (grant agreement No 646908) through ERC Consolidator Grant "S4F". The research of LEK is supported by research grant (19127) from VILLUM FONDEN. HJF gratefully acknowledges the support of STFC for Astrochemistry at the OU under grant Nos ST/P000584/1 and ST/T005424/1 enabling her participation in this work.

Appendix

6.a PRODUCTION OF GAS-PHASE MAPS

6.A.1 *Interferometric and single-dish data combination*

The combined interferometric (SMA) and single-dish (APEX/IRAM 30 m) data were obtained using CASA version 5.6.1 by executing the CASA task `feather`. The `feathering` algorithm consists of Fourier transforming and scaling the single-dish (lower resolution) data to the interferometric (higher resolution) data. In a second step, the two datasets with different spatial resolution are merged. In this work, APEX short-spacing are used to correct the CH_3OH emission detected by SMA observations, whereas the IRAM 30 m short-spacing are folded into the CO isotopologue emissions observed with the SMA. The combination of the interferometric and single-dish datasets was carried out following the procedure described in Appendix 5.B.1 and references therein.

Artefacts might arise when combining interferometric and single dish data. To benchmark our results we have been varying the arguments of the feathering algorithm (e.g., `sdfactor` (scale factor to apply to single dish image), `effdishdiam` (new effective single dish diameter) and `lowpassfiltersd` (filtering out the high spatial frequencies of the single dish image) from the default values. The variations of the above parameters resulted in amplifying the signal close to the primary beam edges by approximately 15%, therefore the default values were chosen.

6.A.2 *Optical depth of the CO isotopologues*

If the emission of the ^{13}CO and C^{18}O isotopologues is co-spatial, the line profiles are similar and the gas ratio abundance ^{12}CO:^{13}CO:C^{18}O is constant, the ^{13}CO optical depth can be assessed from the ^{13}CO and C^{18}O integrated intensity ratio $I(^{13}\mathrm{CO})/I(\mathrm{C}^{18}\mathrm{O})$ using the formalism firstly described by Myers *et al.* (1983) and Ladd *et al.* (1998). The treatment employed here is adapted from Myers *et al.* (1983) and uses formula 6.1 given by e.g., Carlhoff *et al.* (2013) and Zhang *et al.* (2018), relating the integrated intensity ratio of the two isotopologues (Table 6.A.1) and the optical depth τ:

$$\frac{I(^{13}\mathrm{CO})}{I(\mathrm{C}^{18}\mathrm{O})} \approx \frac{1-\exp(-\tau^{^{13}\mathrm{CO}})}{1-\exp(-\tau^{^{13}\mathrm{CO}}/f)}. \tag{6.1}$$

In the above equation $\tau^{^{13}\mathrm{CO}}$ is the ^{13}CO optical depth, and f is the intrinsic ^{13}CO/C^{18}O abundance ratio, which is equal to 7–10 for the Milky Way (Wilson and Matteucci, 1992; Barnes *et al.*, 2015). If f=8 is assumed, to be consistent with the approach adopted in Perotti *et al.* (2020), $\tau^{^{13}\mathrm{CO}}$ is equal to 1.22 for B35A–2, 0.39 for B35–3, 0.47 for B35A–5, and 0.03 for B35–4, indicating ^{13}CO optically thick emission towards three (B35A–2, B35–3 and B35A–5) out of four sources in the B35A cloud as $I(^{13}\mathrm{CO})/I(\mathrm{C}^{18}\mathrm{O})$ is below the intrinsic ratio f for these three sources. The same conclusion is obtained

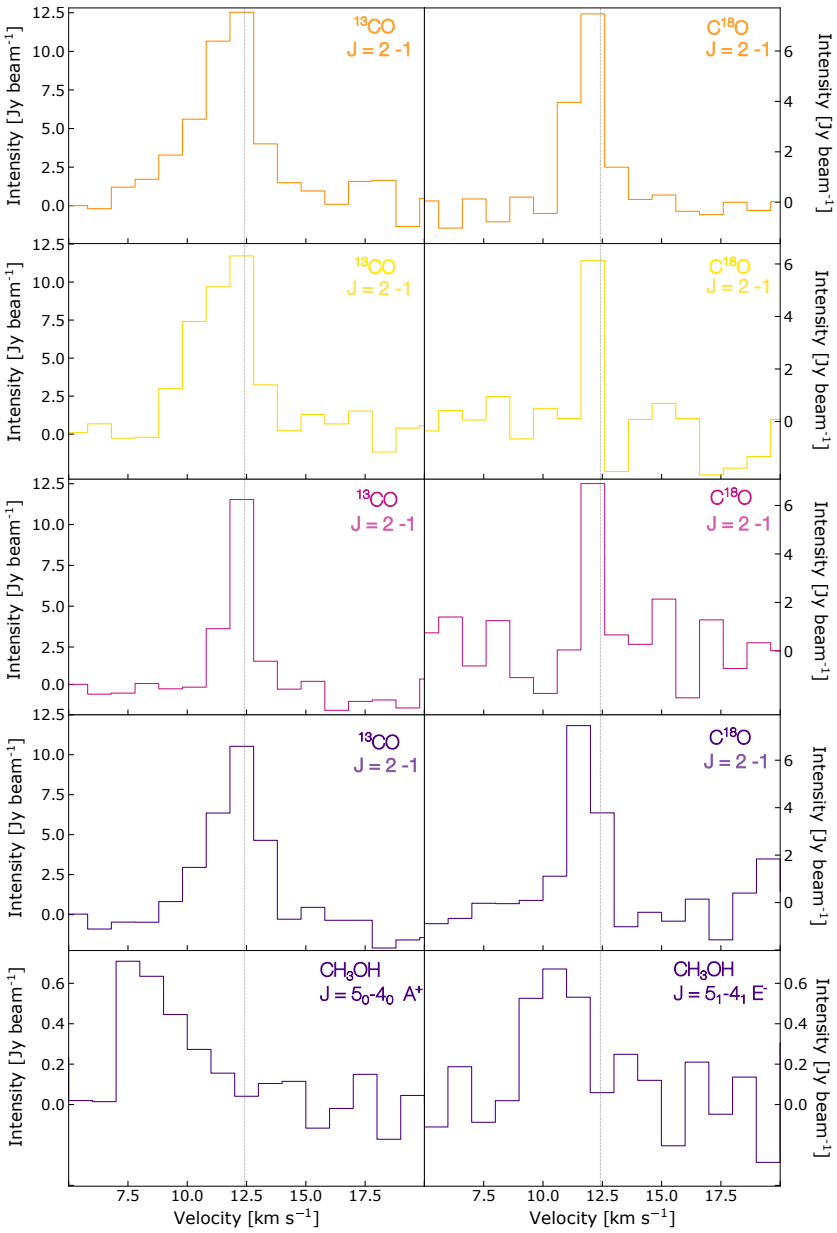

FIGURE 6.A.1: ^{13}CO J=2–1, C^{18}O J=2–1, CH_3OH J=5$_0$–4$_0$ A$^+$ and CH_3OH J=5$_1$–4$_1$ E$^-$ spectra towards the B35A sources detected in the combined interferometric and single-dish data sets. The spectra are colour-coded according to Figure 6.4.2. The cloud velocity (12.42 km s^{-1}) is shown in all spectra with a vertical gray line.

if f=7 or f=10 are assumed. Based on this result, the C^{18}O emission is used to estimate the column densities of ^{12}CO under local thermodynamic equilibrium (LTE) conditions.

6.A.3 *Channel maps and spectra of individual transitions*

Channel maps and spectra for the ^{13}CO J=2–1, C^{18}O J=2–1, and CH_3OH J=5$_0$–4$_0$ A$^+$ detected in the combined interferometric (SMA) and single-dish (IRAM 30m/APEX) data are displayed in Figures 6.A.1, 6.A.3, 6.A.4, and 6.A.5. The CO isotopologue emission is predominantly concentrated towards B35A–2 and B35A–3, whereas the CH_3OH emission is uniquely localised in the vicinity of B35A–5. Blue-shifted components are observed

TABLE 6.A.1: Integrated ^{13}CO and $C^{18}O$ line intensities in units of Jy beam^{-1} km s^{-1} over each source position.

Source	^{13}CO ($J = 2 - 1$)	$C^{18}O$ ($J = 2 - 1$)
B35A–2	70.64 ± 10.59	14.18 ± 2.86
B35A–3	72.36 ± 10.85	10.66 ± 2.17
B35A–4	59.63 ± 8.95	7.55 ± 1.56
B35A–5	70.74 ± 10.61	10.75 ± 2.19

TABLE 6.A.2: Integrated CH_3OH line intensities in units of Jy beam^{-1} km s^{-1} towards B35A–5.

Source	$5_0 - 4_0$ E$^+$	$5_1 - 4_1$ E$^-$	$5_0 - 4_0$ A$^+$	$5_1 - 4_1$ E$^+$	$5_2 - 4_2$ E$^-$
B35A–5	0.27 ± 0.10	0.77 ± 0.18	1.03 ± 0.22	0.29 ± 0.11	0.20 ± 0.09

in combination with broad spectral profiles and wings which deviate from the cloud velocity (12.42 km s^{-1}).

6.A.4 *Derivation of gas-phase column densities*

The column densities of gas-phase species towards the B35A sources were calculated using the integrated intensities of the combined interferometric (SMA) and single-dish (IRAM 30 m/APEX) data (Tables 6.A.1 and 6.A.2). The values inserted in the equations below are listed in Table 6.2.2 and have been taken from the CDMS (Müller *et al.*, 2001), JPL (Pickett *et al.*, 1998) and LAMDA (Schöier *et al.*, 2005) spectral databases. The adopted formalism assumes local thermodynamic equilibrium (LTE) conditions and more specifically, optically thin line emission, homogeneous source filling the telescope beam and that level populations can be described by a single excitation temperature. According to the treatment by Goldsmith and Langer (1999), under the aforementioned conditions, the integrated main-beam temperature $\int T_{\rm MB}\, dv$ and the column density N_u in the upper energy level u are related by:

$$N_u = \frac{8\,\pi\,k_{\rm B}\nu^2}{h\,c^3\,A_{\rm ul}} \int T_{\rm MB}\, dv \tag{6.2}$$

where $k_{\rm B}$ is the Boltzmann's constant, ν is the transition frequency, h is the Planck's constant, c is the speed of light and $A_{\rm ul}$ is the spontaneous Einstein coefficient of the transition. The total column density $N_{\rm tot}$ and the rotational temperature $T_{\rm rot}$ are related to the column density N_u in the upper energy level u (Goldsmith and Langer, 1999) by:

$$\frac{N_u}{g_u} = \frac{N_{\rm tot}}{Q(T_{\rm rot})} e^{-E_u/k_{\rm B}T_{\rm rot}} \tag{6.3}$$

where g_u is the upper level degeneracy, $Q(T_{\rm rot})$ is the rotational partition function, $k_{\rm B}$ is the Boltzmann's constant and E_u is the energy of the upper level u. In summary, the column densities have been calculated using the formalism of Goldsmith and Langer (1999), but assuming a fixed rotational

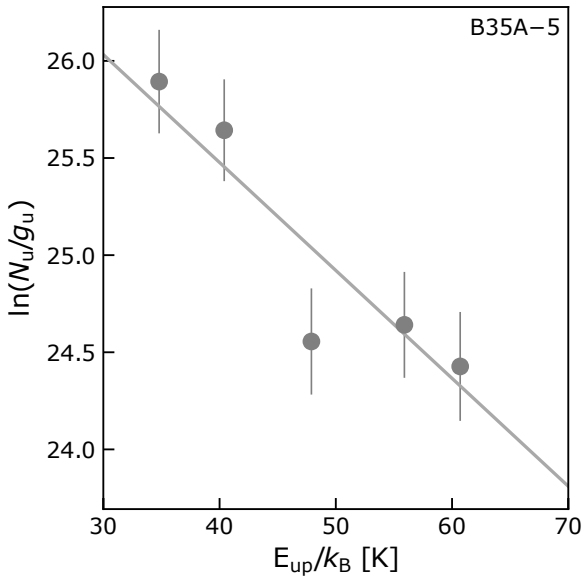

FIGURE 6.A.2: Rotational diagram of CH_3OH for B35A−5. The solid line displays the fixed slope for T_{rot} = 25 K. Error bars are for 1σ uncertainties. The derived column density is shown in Table 6.3.1.

temperature equal to 25 K (Craigon, 2015; Reipurth and Friberg, 2021). Figure 6.A.2 displays the rotational diagram of CH_3OH for B35A−5. Only CH_3OH transitions above 5σ were considered. The uncertainties on the gas column densities were estimated based on the rms noise of the spectra and on the ~20% calibration uncertainty.

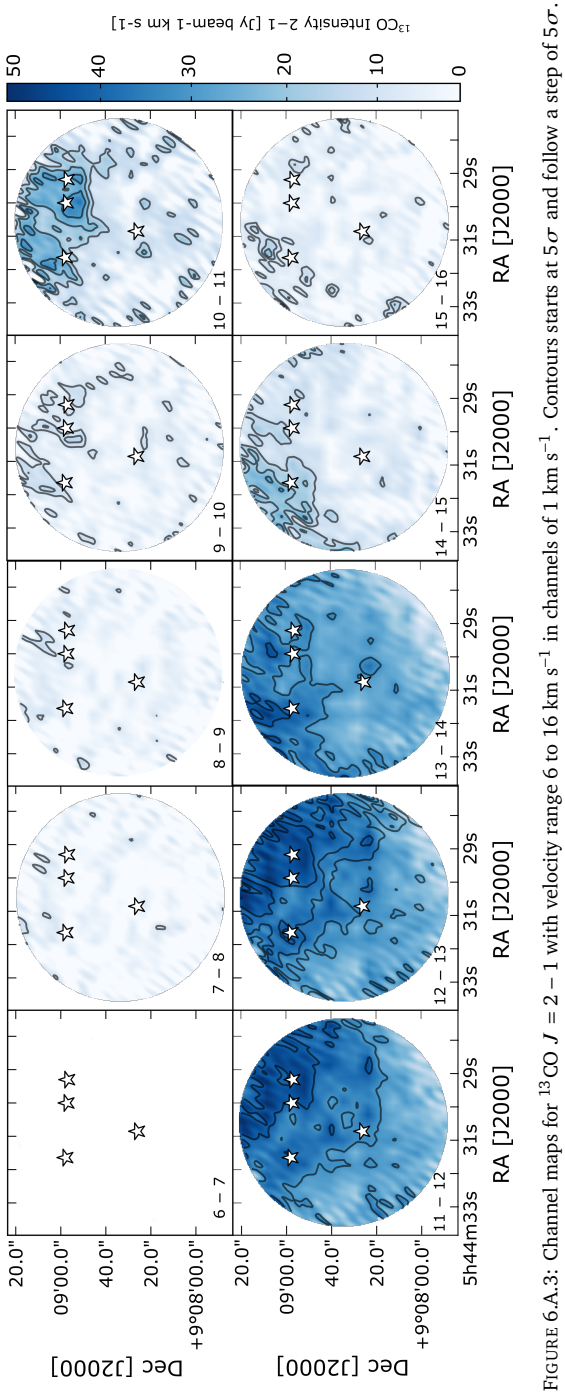

FIGURE 6.A.3: Channel maps for ^{13}CO $J = 2 - 1$ with velocity range 6 to 16 km s^{-1} in channels of 1 km s^{-1}. Contours starts at 5σ and follow a step of 5σ.

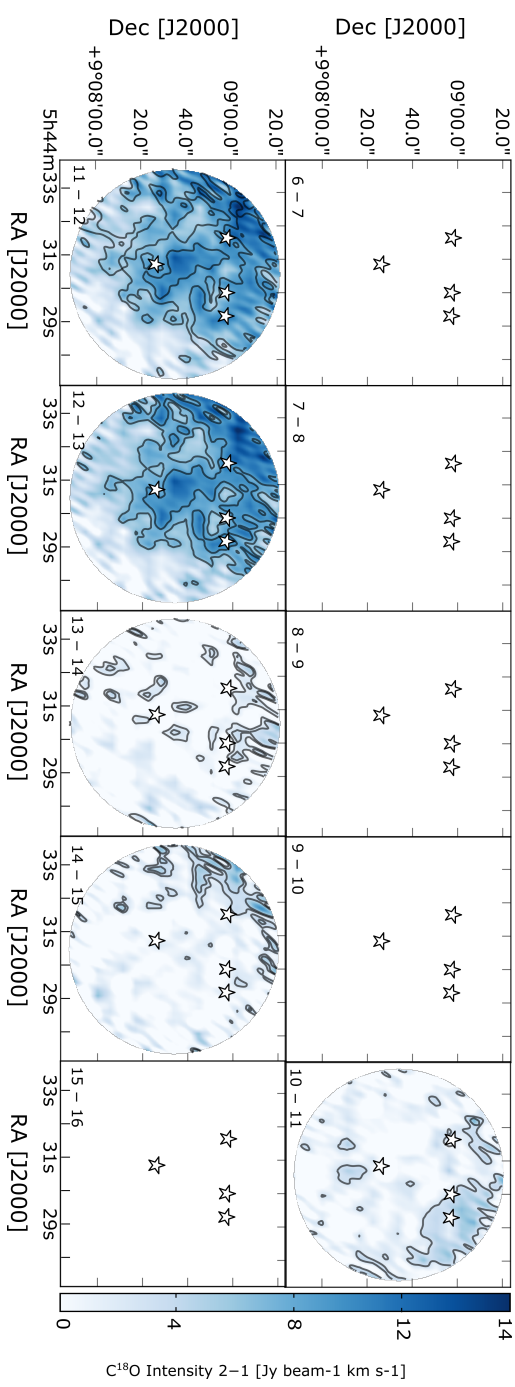

FIGURE 6.A.4: Channel maps for $C^{18}O$ $J = 2 - 1$ with velocity range 6 to 16 km s^{-1} in channels of 1 km s^{-1}. Contours starts at 5σ and follow a step of 5σ.

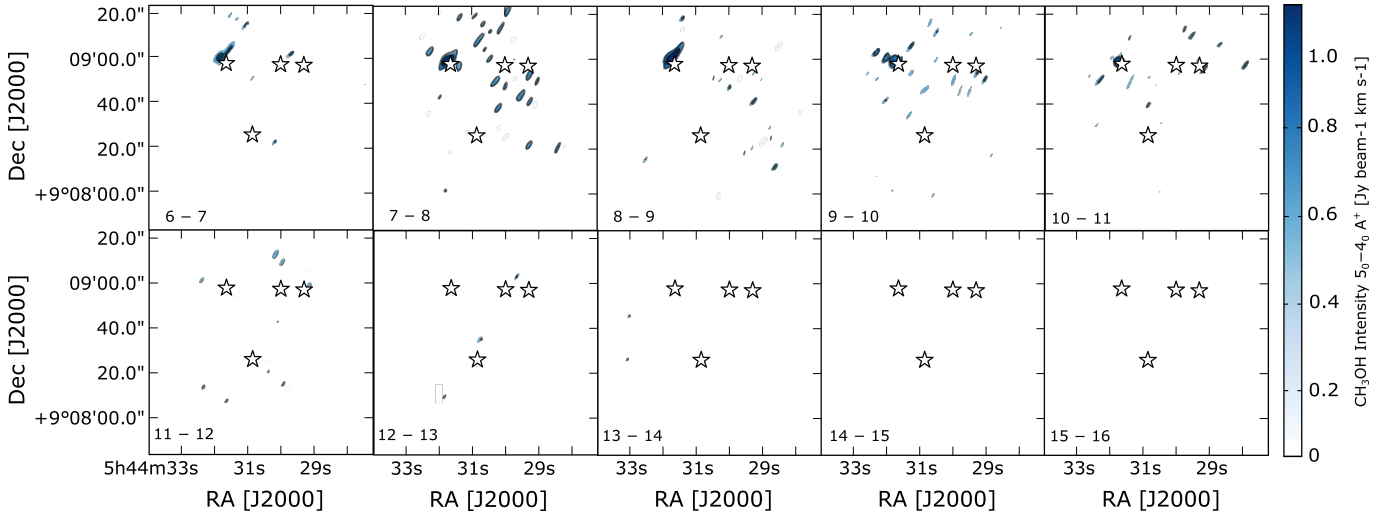

FIGURE 6.A.5: Channel maps for CH_3OH $J = 5_0 - 4_0$ A^+ with velocity range 6 to 16 km s^{-1} in channels of 1 km s^{-1}. Contours starts at 5σ and follow a step of 5σ.

6.b H_2 COLUMN DENSITY FROM VISUAL EXTINCTION

The production of the H_2 column density map is accomplished by using the visual extinction (A_V) values for B35A tabulated in the c2d catalog. No A_V values are reported for B35A−2 and B35A−3 in the catalog. As a result, the visual extinction for B35A−3 is retrieved by de-reddening its spectral energy distribution (SED) at the J, H, K 2MASS photometric points of Table 6.B.1 to fit a first blackbody and fit a second blackbody to model the infrared excess at the IRAC photometric points (see Figure 6.B.1). The extinction in the H-band (A_H) is then calculated using the following equation (Chapman *et al.*, 2009):

$$A_\lambda = -2.5 \log \left[\left(\frac{F_\lambda}{B_\lambda} \right) \left(\frac{1}{\mathrm{k}} \right) \right] \tag{6.4}$$

where λ is the wavelength corresponding in this case to the H-band (1.662 μm), F_λ is the observed flux at the selected λ, k is a scaling factor and B_λ is the blackbody function. The extinction in the H-band is then converted to visual extinction using the equation below:

$$A_V = 5.55 A_H \, (\mathrm{mag}) \tag{6.5}$$

where the conversion factor is taken from Weingartner and Draine (2001). The adopted extinction law takes into account the dust model from Weingartner and Draine (2001) for $R_V = 5.5$ designed for the dense interstellar medium and used by the c2d collaboration (Chapman *et al.*, 2009; Evans *et al.*, 2009). No near-IR photometry data are available for B35A−2, thus the A_V for this source is obtained by interpolating all the tabulated visual

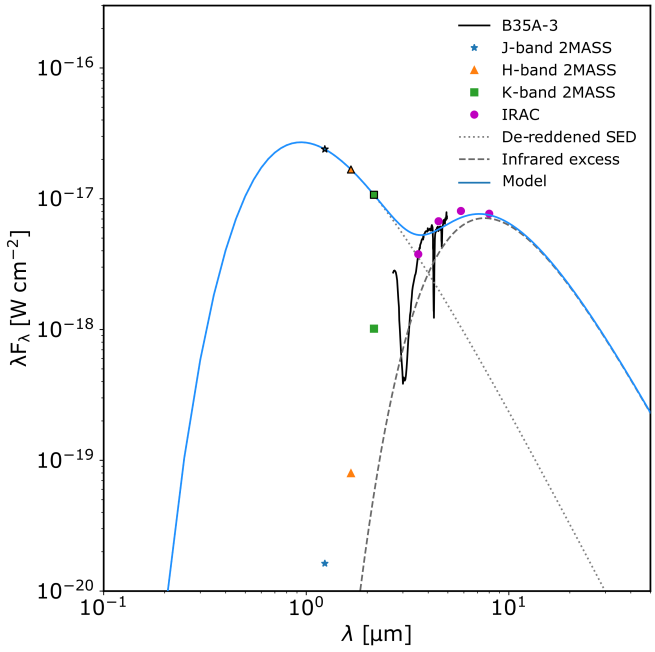

FIGURE 6.B.1: The spectral energy distribution (SED) of B35A−3, which was modeled to determine its visual extinction. The dotted and dashed lines represent the black body functions used to model the stellar component and the infrared excess, respectively. The solid line is the sum of the two contributions.

TABLE 6.B.1: Photometry of B35A–3.

Object	1.235 μm[a] [mJy]	1.662 μm[a] [mJy]	2.159 μm[a] [mJy]	3.6 μm[b] [mJy]
B35A–3	0.067	0.442 ± 0.0871	7.31 ± 0.229	44.59 ± 2.6
	4.5 μm[b] [mJy]	5.8 μm[b] [mJy]	8.0 μm[b] [mJy]	
B35A–3	101 ± 6.9	156 ± 8.09	205 ± 9.97	

Notes. [a] from 2MASS (Skrutskie *et al.*, 2006) [b] from IRAC (Evans *et al.*, 2014).

extinction values for B35A taken from the c2d catalog including the A_V value for B35A–3. The obtained visual extinction map of B35A is then converted to a H_2 column density map using the relation:

$$N_{\mathrm{H_2}} = 1.37 \times 10^{21} \mathrm{cm}^{-2} (A_V / \mathrm{mag}) \tag{6.6}$$

established for dense interstellar medium gas (Evans *et al.*, 2009).

Bibliography

1. ALMA Partnership *et al.*, *ApJ* **808**, L3 (2015).
2. K. Acharyya *et al.*, *A&A* **466**, 1005–1012 (2007).
3. C. M. O. D. Alexander *et al.*, *Geochim. Cosmochim. Acta* **71**, 4380–4403 (2007).
4. V. Allen, M. Cordiner, S. Charnley, *arXiv e-prints* (2020).
5. K. Altwegg *et al.*, *Science Advances* **2**, e1600285–e1600285 (2016).
6. F. O. Alves *et al.*, *ApJ* **904**, L6 (2020).
7. J. Alves, M. Lombardi, C. J. Lada, *A&A* **565**, A18 (2014).
8. S. Andersson, E. F. van Dishoeck, *A&A* **491**, 907–916 (2008).
9. S. Andersson *et al.*, *J. Chem. Phys.* **124**, 064715–064715 (2006).
10. D. P. P. Andrade, M. L. M. Rocco, H. M. Boechat-Roberty, *MNRAS* **409**, 1289–1296 (2010).
11. P. André *et al.*, in *Protostars and Planets VI* (Beuther, Henrik et al., 2014), p. 27.
12. P. André *et al.*, *A&A* **518**, L102 (2010).
13. P. André, *Comptes Rendus Geoscience* **349**, 187–197 (2017).
14. P. Andre, D. Ward-Thompson, M. Barsony, *ApJ* **406**, 122 (1993).
15. S. M. Andrews *et al.*, *ApJ* **869**, L41 (2018).
16. M. Ansdell *et al.*, *AJ* **160**, 248 (Dec. 2020).
17. M. Antiñolo *et al.*, *ApJ* **823**, 25 (2016).
18. E. Artur de la Villarmois *et al.*, *A&A* **626**, A71 (2019).
19. C. R. Arumainayagam *et al.*, *Chemical Society Reviews* **48**, 2293–2314 (2019).
20. Y. Aso *et al.*, *ApJ* **863**, 19 (2018).
21. R. Bachiller *et al.*, *A&A* **295**, L51 (1995).
22. R. Bachiller *et al.*, *A&A* **335**, 266–276 (1998).
23. J. Bally, in *Handbook of Star Forming Regions, Volume I* (Reipurth, B., 2008), vol. 4, p. 459.
24. N. Balucani, C. Ceccarelli, V. Taquet, *MNRAS* **449**, L16–L20 (2015).
25. P. J. Barnes *et al.*, *ApJ* **812**, 6 (2015).
26. D. Barrado *et al.*, *A&A* **526**, A21 (2011).
27. D. Barrado *et al.*, *A&A* **612**, A79 (2018).
28. R. Basalgète *et al.*, *A&A* **647**, A35 (2021).
29. R. Basalgète *et al.*, *A&A* **647**, A36 (2021).
30. M. R. Bate, *MNRAS* **475**, 5618–5658 (2018).
31. A. Bayo *et al.*, *A&A* **536**, A63 (2011).
32. C. P. M. Bell *et al.*, *MNRAS* **434**, 806–831 (2013).
33. C. J. Bennett *et al.*, *ApJ* **660**, 1588–1608 (2007).
34. P. J. Benson, P. C. Myers, *ApJS* **71**, 89 (1989).
35. E. A. Bergin, M. Tafalla, *ARA&A* **45**, 339–396 (2007).
36. J. B. Bergner *et al.*, *ApJ* **841**, 120 (2017).
37. J. B. Bergner *et al.*, *ACS Earth and Space Chemistry* **3**, 1564–1575 (2019).
38. M. Bertin *et al.*, *ApJ* **817**, L12 (2016).
39. E. A. Bibo, P. S. The, D. N. Dawanas, *A&A* **260**, 293–302 (1992).
40. S. E. Bisschop *et al.*, *A&A* **449**, 1297–1309 (2006).
41. L. Bizzocchi *et al.*, *A&A* **569**, A27 (2014).

42. P. Bjerkeli *et al.*, *A&A* **546**, A29 (2012).
43. P. Bjerkeli *et al.*, *A&A* **595**, A39 (2016).
44. R. D. Blandford, D. G. Payne, *MNRAS* **199**, 883–903 (1982).
45. S Blanksby, G Ellison, *Accounts of Chemical Research* **36**, 255–263 (2003).
46. J. Blum, G. Wurm, *ARA&A* **46**, 21–56 (2008).
47. D. Bockelee-Morvan *et al.*, *A&A* **287**, 647–665 (1994).
48. C. F. Bohren, D. R. Huffman, *Absorption and scattering of light by small particles* (New York: Wiley, 1983).
49. A. S. Bolina, W. A. Brown, *Surface Science* **598**, 45–56 (2005).
50. W. B. Bonnor, *ZAp* **39**, 143 (1956).
51. S. Bontemps *et al.*, *A&A* **518**, L85 (2010).
52. A. C. A. Boogert, P. A. Gerakines, D. C. B. Whittet, *ARA&A* **53**, 541–581 (2015).
53. A. C. A. Boogert *et al.*, *A&A* **360**, 683–698 (2000).
54. A. C. A. Boogert *et al.*, *ApJ* **678**, 985–1004 (2008).
55. A. C. A. Boogert *et al.*, *ApJ* **729**, 92 (2011).
56. A. C. A. Boogert *et al.*, *ApJ* **777**, 73 (2013).
57. S. Bottinelli *et al.*, *ApJ* **718**, 1100–1117 (2010).
58. F. Brauer, T. Henning, C. P. Dullemond, *A&A* **487**, L1–L4 (2008).
59. D. Bresnahan *et al.*, *A&A* **615**, A125 (2018).
60. D. S. Briggs, F. R. Schwab, R. A. Sramek, in *Synthesis Imaging in Radio Astronomy II* (Taylor, G. B., Carilli, C. L., and Perley, R. A., 1999), vol. 180, p. 127.
61. T. Y. Brooke, K. Sellgren, T. R. Geballe, *ApJ* **517**, 883–900 (1999).
62. A. Brown, *ApJ* **322**, L31 (1987).
63. V. Buch, R. Czerminski, *J. Chem. Phys.* **95**, 6026–6038 (1991).
64. J. V. Buckle *et al.*, *MNRAS* **399**, 1026–1043 (2009).
65. J. V. Buckle *et al.*, *MNRAS* **422**, 521–541 (2012).
66. J. A. Caballero, *A&A* **478**, 667–674 (2008).
67. H. Calcutt *et al.*, *A&A* **616**, A90 (2018).
68. L. Cambrésy, *A&A* **345**, 965–976 (1999).
69. J. A. Cardelli, G. C. Clayton, J. S. Mathis, *ApJ* **345**, 245 (1989).
70. P. Carlhoff *et al.*, *A&A* **560**, A24 (2013).
71. J. M. Carpenter, *AJ* **120**, 3139–3161 (2000).
72. M. M. Casali, C. Eiroa, W. D. Duncan, *A&A* **275**, 195–200 (1993).
73. S. Cazaux *et al.*, *ApJ* **593**, L51–L55 (2003).
74. S. Cazaux *et al.*, *A&A* **585**, A55 (2016).
75. S. Cazaux *et al.*, *ApJ* **849**, 80 (2017).
76. P. Cazzoletti *et al.*, *A&A* **626**, A11 (2019).
77. C. J. Chandler, J. E. Carlstrom, *ApJ* **466**, 338 (1996).
78. N. L. Chapman *et al.*, *ApJ* **690**, 496–511 (2009).
79. S. B. Charnley, A. G. G. M. Tielens, S. D. Rodgers, *ApJ* **482**, L203–L206 (1997).
80. S. B. Charnley, in *IAU Colloq. 161: Astronomical and Biochemical Origins and the Search for Life in the Universe* (Batalli Cosmovici, Cristiano, Bowyer, Stuart, and Werthimer, Dan, 1997), p. 89.
81. H. Chen *et al.*, *ApJ* **445**, 377 (1995).
82. X. Chen, H. G. Arce, *ApJ* **720**, L169–L173 (2010).
83. J. E. Chiar *et al.*, *ApJ* **426**, 240 (1994).
84. J. E. Chiar *et al.*, *ApJ* **570**, 198–209 (2002).
85. J. E. Chiar *et al.*, *ApJ* **731**, 9 (2011).

86. M. Choi, *ApJ* **705**, 1730–1734 (2009).
87. L. E. U. Chu, K. Hodapp, A. Boogert, *ApJ* **904**, 86 (2020).
88. K. J. Chuang *et al.*, *MNRAS* **455**, 1702–1712 (2016).
89. K. J. Chuang *et al.*, *MNRAS* **467**, 2552–2565 (2017).
90. A. Ciaravella *et al.*, *Proceedings of the National Academy of Science* **117**, 16149–16153 (2020).
91. M. P. Collings *et al.*, *ApJ* **583**, 1058–1062 (2003).
92. M. P. Collings *et al.*, *MNRAS* **354**, 1133–1140 (2004).
93. M. S. Connelley, B. Reipurth, A. T. Tokunaga, *AJ* **135**, 2496–2525 (2008).
94. P. S. Conti, E. M. Leep, *ApJ* **193**, 113–124 (1974).
95. A. M. Craigon, http://digitool.lib.strath.ac.uk/R/?func=dbin-jump-full&object_id=27550, PhD thesis, Dept. of Physics, Univ. of Strathclyde, 2015.
96. G. A. Cruz-Diaz *et al.*, *A&A* **592**, A68 (2016).
97. H. M. Cuppen, E. Herbst, *ApJ* **668**, 294–309 (2007).
98. H. M. Cuppen *et al.*, *MNRAS* **417**, 2809–2816 (2011).
99. H. M. Cuppen *et al.*, *Space Sci. Rev.* **212**, 1–58 (2017).
100. A. Dalgarno, in, ed. by B. Bederson, A. Dalgarno (Academic Press, 1994), vol. 32, pp. 57–68.
101. T. M. Dame, P. Thaddeus, *ApJ* **297**, 751–765 (1985).
102. T. M. Dame *et al.*, *ApJ* **322**, 706 (1987).
103. E. Dartois *et al.*, *A&A* **618**, A173 (2018).
104. E. Dartois *et al.*, *Astronomy and Astrophysics* **627**, A55 (2019).
105. E. Dartois *et al.*, *A&A* **634**, A103 (2020).
106. A. Das *et al.*, *ApJS* **237**, 9 (2018).
107. C. J. Davis *et al.*, *MNRAS* **309**, 141–152 (1999).
108. A. Dawes, N. J. Mason, H. J. Fraser, *Phys. Chem. Chem. Phys.* **18**, 1245–1257 (2 2016).
109. C. H. De Vries, G. Narayanan, R. L. Snell, *ApJ* **577**, 798–825 (2002).
110. J. T. Dempsey *et al.*, *MNRAS* **430**, 2534–2544 (2013).
111. J. P. Devlin, *J. Chem. Phys* **96**, 6185–6188 (1992).
112. J. Di Francesco *et al.*, *ApJS* **175**, 277–295 (2008).
113. S. Dib, T. Henning, *A&A* **629**, A135 (2019).
114. O. Dionatos *et al.*, *A&A* **558**, A88 (2013).
115. O. Dionatos *et al.*, *A&A* **563**, A28 (2014).
116. C. J. Dolan, R. D. Mathieu, *AJ* **118**, 2409–2423 (1999).
117. C. J. Dolan, R. D. Mathieu, *AJ* **123**, 387–403 (2002).
118. B. T. Draine, *ARA&A* **41**, 241–289 (2003).
119. B. T. Draine, F. Bertoldi, *ApJ* **468**, 269 (1996).
120. M. N. Drozdovskaya *et al.*, *MNRAS* **490**, 50–79 (2019).
121. A. Duarte-Cabral *et al.*, *A&A* **519**, A27 (2010).
122. F. Dulieu *et al.*, *Scientific Reports* **3**, 1338 (2013).
123. M. M. Dunham *et al.*, in *Protostars and Planets VI* (Beuther, Henrik et al., 2014), p. 195.
124. M. M. Dunham *et al.*, *ApJS* **220**, 11 (2015).
125. R. Dupuy *et al.*, *Nature Astronomy* **2**, 796–801 (2018).
126. A. Duquennoy, M. Mayor, *A&A* **500**, 337–376 (1991).
127. R. Ebert, *ZAp* **37**, 217 (1955).
128. P. Ehrenfreund, S. B. Charnley, *ARA&A* **38**, 427–483 (2000).
129. C. Eiroa, M. M. Casali, *A&A* **223**, L17–L19 (1989).

130. C. Eiroa, A. A. Djupvik, M. M. Casali, in *Handbook of Star Forming Regions, Volume II: The Southern Sky ASP Monograph Publications* (Reipurth, B. ed, 2008), vol. 5, p. 693.
131. C. Eistrup, C. Walsh, E. F. van Dishoeck, *A&A* **595**, A83 (2016).
132. D. D. Eley, E. K. Rideal, *Nature* **146**, 401–402 (1940).
133. I. Evans Neal J. *et al.*, *ApJS* **181**, 321–350 (2009).
134. N. J. Evans II *et al.*, *VizieR Online Data Catalog* **2332** (2014).
135. E. C. Fayolle *et al.*, *ApJ* **739**, L36 (2011).
136. E. C. Fayolle *et al.*, *ApJ* **816**, L28 (2016).
137. G. G. Fazio *et al.*, *ApJS* **154**, 10–17 (2004).
138. G. Fedoseev *et al.*, *MNRAS* **448**, 1288–1297 (2015).
139. G. Fedoseev *et al.*, *MNRAS* **446**, 439–448 (2015).
140. G. Fedoseev *et al.*, *ApJ* **842**, 52 (2017).
141. S. Ferrero *et al.*, *ApJ* **904**, 11 (2020).
142. J. Forbrich, T. Preibisch, *A&A* **475**, 959–972 (2007).
143. J. Forbrich *et al.*, *A&A* **464**, 1003–1013 (2007).
144. D. Foreman-Mackey *et al.*, *PASP* **125**, 306 (2013).
145. H. J. Fraser, E. F. van Dishoeck, *Advances in Space Research* **33**, 14–22 (2004).
146. H. J. Fraser *et al.*, *MNRAS* **327**, 1165–1172 (2001).
147. H. J. Fraser *et al.*, *MNRAS* **353**, 59–68 (2004).
148. S. Frimann, J. K. Jørgensen, T. Haugbølle, *A&A* **587**, A59 (2016).
149. G. W. Fuchs *et al.*, *A&A* **505**, 629–639 (2009).
150. P. A. B. Galli *et al.*, *A&A* **634**, A98 (2020).
151. R. T. Garrod, E. Herbst, *A&A* **457**, 927–936 (2006).
152. R. T. Garrod, V. Wakelam, E. Herbst, *A&A* **467**, 1103–1115 (2007).
153. R. T. Garrod, S. L. Widicus Weaver, E. Herbst, *ApJ* **682**, 283–302 (2008).
154. W. D. Geppert *et al.*, *Faraday Discussions* **133**, 177 (2006).
155. P. A. Gerakines *et al.*, *A&A* **296**, 810 (1995).
156. G. Giardino *et al.*, *A&A* **463**, 275–288 (2007).
157. E. L. Gibb *et al.*, *ApJS* **151**, 35–73 (2004).
158. B. M. Giuliano *et al.*, *A&A* **592**, A81 (2016).
159. P. F. Goldsmith, W. D. Langer, *ApJ* **517**, 209–225 (1999).
160. M. Goto *et al.*, *arXiv e-prints* (2020).
161. R. J. Gould, E. E. Salpeter, *ApJ* **138**, 393 (1963).
162. L. V. Gramajo *et al.*, *AJ* **139**, 2504–2524 (2010).
163. T. Grassi *et al.*, *A&A* **643**, A155 (Nov. 2020).
164. R. O. Gray *et al.*, *AJ* **132**, 161–170 (2006).
165. G. M. Green *et al.*, *ApJ* **810**, 25 (2015).
166. M. J. Griffin *et al.*, *A&A* **518**, L3 (2010).
167. R. J. A. Grim *et al.*, *A&A* **243**, 473 (1991).
168. C. E. Groppi *et al.*, *ApJ* **670**, 489–498 (2007).
169. W. M. Grundy *et al.*, *Science* **367**, aay3705 (2020).
170. R. Güsten *et al.*, *A&A* **454**, L13–L16 (2006).
171. R. A. Gutermuth *et al.*, *ApJ* **673**, L151 (2008).
172. W. Hagen, L. J. Allamandola, J. M. Greenberg, *A&A* **86**, L3–L6 (1980).
173. G. Haro, *ApJ* **115**, 572 (1952).

174. J. Harris, B. Kasemo, *Surface Science* **105**, L281–L287 (1981).
175. D. Harsono *et al.*, *A&A* **562**, A77 (2014).
176. D. Harsono *et al.*, *Nature Astronomy* **2**, 646–651 (2018).
177. P. Hartigan, J. A. Graham, *AJ* **93**, 913 (1987).
178. P. Harvey *et al.*, *ApJ* **663**, 1149–1173 (2007).
179. T. I. Hasegawa, E. Herbst, *MNRAS* **263**, 589 (1993).
180. T. I. Hasegawa, E. Herbst, C. M. Leung, *ApJS* **82**, 167 (1992).
181. T. Hassenkam *et al.*, *Nature* **548**, 78–81 (2017).
182. T. J. Haworth *et al.*, *MNRAS* **501**, 3502–3514 (2021).
183. C. Heiles, H. J. Habing, *A&AS* **14**, 1 (1974).
184. T. T. Helfer *et al.*, *ApJS* **145**, 259–327 (2003).
185. T. Henning, *ARA&A* **48**, 21–46 (2010).
186. T. Henning, G. Meeus, in *Physical Processes in Circumstellar Disks around Young Stars* (Garcia, Paulo J. V., 2011), pp. 114–148.
187. G. H. Herbig, *Vistas in Astronomy* **8**, 109–125 (1966).
188. G. H. Herbig, *ApJ* **111**, 11 (1950).
189. G. H. Herbig, *ApJS* **4**, 337 (1960).
190. E. Herbst, W. Klemperer, *ApJ* **185**, 505–534 (1973).
191. E. Herbst, C. M. Leung, *ApJS* **69**, 271 (1989).
192. E. Herbst, E. F. van Dishoeck, *ARA&A* **47**, 427–480 (2009).
193. G. J. Herczeg *et al.*, *ApJ* **849**, 43 (2017).
194. G. J. Herczeg *et al.*, *ApJ* **878**, 111 (2019).
195. J. Hernández *et al.*, *ApJ* **662**, 1067–1081 (2007).
196. J. Hernández *et al.*, *ApJ* **707**, 705–715 (2009).
197. J. Hernández *et al.*, *ApJ* **794**, 36 (2014).
198. M. Heyer, T. M. Dame, *ARA&A* **53**, 583–629 (2015).
199. C. N. Hinshelwood, in (Oxford University Press, 1940), pp. 36–39.
200. P. T. P. Ho, J. M. Moran, K. Y. Lo, *ApJ* **616**, L1–L6 (2004).
201. S. Hoban *et al.*, *Icarus* **105**, 548–556 (1993).
202. J. A. Högbom, *A&AS* **15**, 417 (1974).
203. D. J. Hollenbach, A. G. G. M. Tielens, *Reviews of Modern Physics* **71**, 173–230 (1999).
204. D. Hollenbach, C. F. McKee, *ApJ* **342**, 306 (1989).
205. D. Hollenbach, E. E. Salpeter, *ApJ* **163**, 155 (1971).
206. M. Honda *et al.*, *ApJ* **690**, L110–L113 (2009).
207. D. M. Hudgins *et al.*, *ApJS* **86**, 713–870 (1993).
208. C. L. H. Hull *et al.*, *ApJ* **847**, 92 (2017).
209. R. L. Hurt, M. Barsony, *ApJ* **460**, L45 (1996).
210. S. Ioppolo *et al.*, *ApJ* **686**, 1474–1479 (2008).
211. S. Ioppolo *et al.*, *MNRAS* **413**, 2281–2287 (2011).
212. S. Ioppolo *et al.*, *A&A* **646**, A172 (2021).
213. M. Ishii *et al.*, *AJ* **124**, 2790–2798 (2002).
214. J. H. Jeans, *Philosophical Transactions of the Royal Society of London Series A* **199**, 1–53 (1902).
215. R. D. Jeffries, *MNRAS* **376**, 1109–1119 (2007).
216. A. Jiménez-Escobar *et al.*, *ApJ* **820**, 25 (2016).
217. A. Jiménez-Escobar *et al.*, *ApJ* **868**, 73 (2018).

218. I. Jiménez-Serra *et al.*, *A&A* **482**, 549–559 (2008).
219. I. Jiménez-Serra *et al.*, *Astrobiology* **20**, 1048–1066 (2020).
220. D. Johnstone *et al.*, *ApJ* **559**, 307–317 (2001).
221. J. K. Jørgensen *et al.*, *A&A* **415**, 1021–1037 (2004).
222. J. K. Jørgensen *et al.*, *A&A* **595**, A117 (2016).
223. J. K. Jørgensen, A. Belloche, R. T. Garrod, *ARA&A* **58**, 727–778 (2020).
224. G. Jungclaus *et al.*, *Meteoritics* **11**, 231–237 (1976).
225. J. Kauffmann *et al.*, *A&A* **487**, 993–1017 (2008).
226. J. V. Keane *et al.*, *A&A* **376**, 254–270 (2001).
227. M. Keppler *et al.*, *A&A* **617**, A44 (2018).
228. G. Kim *et al.*, *ApJS* **249**, 33 (2020).
229. R. F. Knacke *et al.*, *ApJ* **179**, 847–854 (1973).
230. C. Knez *et al.*, *ApJ* **635**, L145–L148 (2005).
231. J. Koda *et al.*, *ApJS* **193**, 19 (2011).
232. K. W. Kolasinski, in (Wiley, J. & Sons Ltd., Chichester, England, 1st Ed., 2002).
233. V. Könyves *et al.*, *A&A* **584**, A91 (2015).
234. M. Kounkel, *ApJ* **902**, 122 (2020).
235. M. Kounkel *et al.*, *AJ* **156**, 84 (2018).
236. L. E. Kristensen, M. M. Dunham, *A&A* **618**, A158 (2018).
237. L. E. Kristensen *et al.*, *A&A* **516**, A57 (2010).
238. M. Kuffmeier, B. Zhao, P. Caselli, *A&A* **639**, A86 (2020).
239. M. Kuffmeier, T. Haugbølle, Å. Nordlund, *ApJ* **846**, 7 (2017).
240. Y. Kurono, K.-I. Morita, T. Kamazaki, *PASJ* **61**, 873 (2009).
241. C. J. Lada, J. H. Black, *ApJ* **203**, L75–L79 (1976).
242. C. J. Lada, in *Star Forming Regions* (Peimbert, Manuel and Jugaku, Jun, 1987), vol. 115, p. 1.
243. E. F. Ladd, G. A. Fuller, J. R. Deane, *ApJ* **495**, 871–890 (1998).
244. W. J. Lang *et al.*, *A&A* **357**, 1001–1012 (2000).
245. P. Langevin, *J. Phys. Theor. Appl.* **4**, 678 (1905).
246. I. Langmuir, *Trans. Faraday Soc.* **17**, 607–620 (1922).
247. B. Larsson *et al.*, *A&A* **363**, 253–268 (2000).
248. L. Le Roy *et al.*, *A&A* **583**, A1 (2015).
249. H. H. Lee *et al.*, *A&A* **311**, 690–707 (1996).
250. H.-T. Lee *et al.*, *ApJ* **624**, 808–820 (2005).
251. K. I. Lee *et al.*, *ApJ* **797**, 76 (2014).
252. K. Levenberg, *Quart. Appl. Math.* **2**, 164–168 (1944).
253. Y. Lin *et al.*, *ApJ* **840**, 22 (2017).
254. J. E. Lindberg, J. K. Jørgensen, *A&A* **548**, A24 (2012).
255. J. E. Lindberg *et al.*, *A&A* **584**, A28 (2015).
256. J. E. Lindberg *et al.*, *A&A* **566**, A74 (2014).
257. J. E. Lindberg *et al.*, *ApJ* **835**, 3 (2017).
258. H. Linnartz, S. Ioppolo, G. Fedoseev, *International Reviews in Physical Chemistry* **34**, 205–237 (2015).
259. T. Liu *et al.*, *ApJS* **222**, 7 (2016).
260. R. Lüst, A. Schlüter, *ZAp* **38**, 190 (1955).
261. M.-M. Mac Low, R. S. Klessen, *Reviews of Modern Physics* **76**, 125–194 (2004).
262. R. J. Maddalena, M. Morris, *ApJ* **323**, 179 (1987).

263. E. E. Mamajek, in *Exoplanets and Disks: Their Formation and Diversity* (Usuda, Tomonori, Tamura, Motohide, and Ishii, Miki, 2009), vol. 1158, pp. 3–10.

264. E. E. Mamajek, M. R. Meyer, J. Liebert, *AJ* **124**, 1670–1694 (2002).

265. S. Manigand *et al.*, *A&A* **635**, A48 (2020).

266. D. Marquardt, *J. Soc. Indust. Appl. Math.* **11**, 431–441 (1963).

267. R. Martín-Doménech, G. M. Muñoz Caro, G. A. Cruz-Díaz, *A&A* **589**, A107 (2016).

268. R. Martín-Doménech *et al.*, *ApJ* **880**, 130 (2019).

269. R. D. Mathieu, in *in Handbook of Star Forming Regions, Volume I. The Northern Sky* (Reipurth, B. ed, 2008), vol. 4, ASP Monographs, p. 757.

270. A. J. Maury *et al.*, *A&A* **621**, A76 (2019).

271. B. A. McGuire, *ApJS* **239**, 17 (2018).

272. J. P. McMullin *et al.*, in *Astronomical Data Analysis Software and Systems XVI* (Shaw, R. A., Hill, F., and Bell, D. J., 2007), vol. 376, p. 127.

273. J. P. McMullin *et al.*, *ApJ* **424**, 222 (1994).

274. J. P. McMullin *et al.*, *ApJ* **536**, 845–856 (2000).

275. S. T. Megeath *et al.*, *AJ* **144**, 192 (2012).

276. S. T. Megeath *et al.*, *AJ* **151**, 5 (2016).

277. C. Meinert *et al.*, *Science* **352**, 208–212 (2016).

278. K. M. Menten *et al.*, *A&A* **474**, 515–520 (2007).

279. D. Mesa *et al.*, *A&A* **624**, A4 (2019).

280. L. Mestel, *MNRAS* **138**, 359 (1968).

281. O. Miettinen *et al.*, *A&A* **486**, 799–806 (2008).

282. M. Minissale *et al.*, *A&A* **585**, A24 (2016).

283. M. Minissale *et al.*, *MNRAS* **458**, 2953–2961 (2016).

284. N. Miyauchi *et al.*, *Chemical Physics Letters* **456**, 27–30 (2008).

285. P. Modica, M. E. Palumbo, G. Strazzulla, *Planet. Space Sci.* **73**, 425–429 (2012).

286. S. J. Mojzsis *et al.*, *Nature* **384**, 55–59 (1996).

287. L. K. Morgan *et al.*, *A&A* **477**, 557–571 (2008).

288. J. C. Mottram *et al.*, *A&A* **600**, A99 (2017).

289. J. Moultaka *et al.*, *A&A* **425**, 529–542 (2004).

290. G. M. Muñoz Caro *et al.*, *ACS Earth and Space Chemistry* **3**, 2138–2157 (2019).

291. H. S. P. Müller *et al.*, *A&A* **370**, L49–L52 (2001).

292. M. J. Mumma, S. B. Charnley, *ARA&A* **49**, 471–524 (2011).

293. K. Murakawa, M. Tamura, T. Nagata, *ApJS* **128**, 603–613 (2000).

294. P. Murdin, M. V. Penston, *MNRAS* **181**, 657 (1977).

295. N. M. Murillo *et al.*, *A&A* **592**, A56 (2016).

296. P. C. Myers, E. F. Ladd, *ApJ* **413**, L47 (1993).

297. P. C. Myers, R. A. Linke, P. J. Benson, *ApJ* **264**, 517–537 (1983).

298. P. C. Myers *et al.*, *ApJ* **324**, 907 (1988).

299. P. C. Myers, *ApJ* **700**, 1609–1625 (2009).

300. F. Nakamura *et al.*, *ApJ* **837**, 154 (2017).

301. J. Nelder, R. Mead, *The Computer Journal* **7**, 308 (1965).

302. D. A. Neufeld, A. Dalgarno, *ApJ* **340**, 869 (1989).

303. R. Neuhäuser, J. Forbrich, in *Handbook of Star Forming Regions, Volume II* (Reipurth, B., 2008), vol. 5, p. 735.

304. R. Neuhäuser *et al.*, *A&AS* **146**, 323–347 (2000).

305. B. Nisini *et al.*, *A&A* **518**, L120 (2010).

306. J. A. Noble *et al.*, *MNRAS* **421**, 768–779 (2012).
307. J. A. Noble *et al.*, *ApJ* **775**, 85 (2013).
308. J. A. Noble *et al.*, *Monthly Notices of the Royal Astronomical Society* **467**, 4753–4762 (2017).
309. J. A. Noble, PhD thesis, Dept. of Physics, Univ. of Strathclyde, 2011.
310. M. Nuevo, G. Cooper, S. A. Sandford, *Nature Communications* **9**, 5276 (2018).
311. D. J. Nutter, D. Ward-Thompson, P. André, *MNRAS* **357**, 975–982 (2005).
312. K. I. Öberg, S. Bottinelli, E. F. van Dishoeck, *A&A* **494**, L13–L16 (2009).
313. K. I. Öberg *et al.*, *ApJ* **621**, L33–L36 (2005).
314. K. I. Öberg *et al.*, *A&A* **504**, 891–913 (2009).
315. K. I. Öberg *et al.*, *ApJ* **740**, 109 (2011).
316. K. I. Öberg, *Chemical Reviews* **116**, 9631–9663 (2016).
317. K. I. Öberg, E. A. Bergin, *Phys. Rep.* **893**, 1–48 (2021).
318. K. I. Öberg, R. Murray-Clay, E. A. Bergin, *ApJ* **743**, L16 (2011).
319. K. I. Öberg *et al.*, *ApJ* **740**, 14 (2011).
320. T. Oka, *Proceedings of the National Academy of Science* **103**, 12235–12242 (2006).
321. G. N. Ortiz-León *et al.*, *ApJ* **869**, L33 (2018).
322. V. Ossenkopf, T. Henning, *A&A* **291**, 943–959 (1994).
323. P. Padoan, Å. Nordlund, *ApJ* **576**, 870–879 (2002).
324. Y. J. Pendleton, A. G. G. M. Tielens, M. W. Werner, *ApJ* **349**, 107 (1990).
325. E. M. Penteado, C. Walsh, H. M. Cuppen, *ApJ* **844**, 71 (2017).
326. G. Perotti *et al.*, *A&A* **643**, A48 (2020).
327. G. Perotti *et al.*, *A&A* **650**, A168 (2021).
328. D. E. Peterson *et al.*, *ApJS* **194**, 43 (2011).
329. H. M. Pickett *et al.*, *J. Quant. Spectr. Rad. Transf.* **60**, 883–890 (1998).
330. J. B. Pickles, D. A. Williams, *Ap&SS* **52**, 443–452 (1977).
331. M. Planck, *Verhandl. Dtsch. phys. Ges.* **2**, 202 (1900).
332. D. Polychroni *et al.*, *ApJ* **777**, L33 (2013).
333. K. M. Pontoppidan, *A&A* **453**, L47–L50 (2006).
334. K. M. Pontoppidan, S. M. Blevins, *Faraday Discussions* **168**, 49–60 (2014).
335. K. M. Pontoppidan, E. F. van Dishoeck, E. Dartois, *A&A* **426**, 925–940 (2004).
336. K. M. Pontoppidan *et al.*, *A&A* **408**, 981–1007 (2003).
337. K. M. Pontoppidan *et al.*, *A&A* **404**, L17–L20 (2003).
338. K. M. Pontoppidan *et al.*, *ApJ* **678**, 1005–1031 (2008).
339. K. M. Pontoppidan *et al.*, in *Protostars and Planets VI* (Beuther, Henrik et al., 2014), p. 363.
340. K. M. Pontoppidan *et al.*, *ApJ* **874**, 92 (2019).
341. M. S. Povich *et al.*, *ApJS* **209**, 31 (2013).
342. T. Preibisch, *A&A* **410**, 951–959 (2003).
343. T. Preibisch, *A&A* **428**, 569–577 (2004).
344. R. E. Pudritz, T. P. Ray, *Frontiers in Astronomy and Space Sciences* **6**, 54 (2019).
345. D. Qasim *et al.*, *A&A* **612**, A83 (2018).
346. D. Qasim *et al.*, *Nature Astronomy* **4**, 781–785 (2020).
347. S.-L. Qin, Y.-F. Wu, *Chinese J. Astron. Astrophys.* **3**, 69–74 (2003).
348. D. Rabli, D. R. Flower, *MNRAS* **406**, 95–101 (2010).
349. F. R. S. Rayleigh, *XXXI. Investigations in optics, with special reference to the spectroscope*, 1879.
350. P. Redondo, C. Barrientos, A. Largo, *ApJ* **836**, 240 (2017).

351. P. Redondo *et al.*, *A&A* **603**, A139 (2017).
352. B. Reipurth, *VizieR Online Data Catalog*, V/104 (2000).
353. B. Reipurth, J. Bally, *ARA&A* **39**, 403–455 (2001).
354. B. Reipurth, P. Friberg, *MNRAS* **501**, 5938–5947 (2021).
355. V. M. Rivilla *et al.*, *MNRAS* **483**, L114–L119 (2019).
356. H. Roberts, T. J. Millar, *A&A* **361**, 388–398 (2000).
357. T. P. Robitaille, *A&A* **600**, A11 (2017).
358. T. P. Robitaille *et al.*, *ApJS* **169**, 328–352 (2007).
359. T. P. Robitaille *et al.*, *ApJS* **167**, 256–285 (2006).
360. W. R. M. Rocha, S. Pilling, *ApJ* **803**, 18 (2015).
361. K. Rohlfs, T. L. Wilson, *Tools of Radio Astronomy* (Springer Verlag, 1996).
362. G. S. Rossano, *AJ* **83**, 234–240 (1978).
363. L. S. Rothman *et al.*, *Appl. Opt.* **26**, 4058–4097 (1987).
364. M. Rubin *et al.*, *MNRAS* **489**, 594–607 (2019).
365. D. P. Ruffle, E. Herbst, *MNRAS* **322**, 770–778 (2001).
366. D. P. Ruffle, E. Herbst, *MNRAS* **324**, 1054–1062 (2001).
367. D. Rumble *et al.*, *MNRAS* **448**, 1551–1573 (2015).
368. M. Sahan, L. M. Haffner, *AJ* **151**, 147 (2016).
369. G. Santangelo *et al.*, *A&A* **538**, A45 (2012).
370. S. L. Schnee *et al.*, *ApJ* **634**, 442–450 (2005).
371. S. Schneider, B. G. Elmegreen, *ApJS* **41**, 87–95 (1979).
372. F. L. Schöier *et al.*, *A&A* **390**, 1001–1021 (2002).
373. F. L. Schöier *et al.*, *A&A* **432**, 369–379 (2005).
374. F. L. Schöier *et al.*, *A&A* **454**, L67–L70 (2006).
375. W. A. Schutte *et al.*, *A&A* **343**, 966–976 (1999).
376. D. M. Segura-Cox *et al.*, *ApJ* **866**, 161 (2018).
377. D. M. Segura-Cox *et al.*, *Nature* **586**, 228–231 (2020).
378. R. J. Shannon *et al.*, *Nature Chemistry* **5**, 745–749 (2013).
379. R. J. Shannon *et al.*, *RSC Advances* **4**, 26342–26353 (2014).
380. S. Sharpless, *ApJS* **4**, 257 (1959).
381. T. Shimonishi *et al.*, *ApJ* **855**, 27 (2018).
382. F. H. Shu, *ApJ* **214**, 488–497 (1977).
383. M. A. J. Simons, T. Lamberts, H. M. Cuppen, *A&A* **634**, A52 (2020).
384. D. Skouteris *et al.*, *ApJ* **854**, 135 (2018).
385. M. F. Skrutskie *et al.*, *AJ* **131**, 1163–1183 (2006).
386. L. Song, J. Kästner, *ApJ* **850**, 118 (2017).
387. S. Spezzano *et al.*, *A&A* **643**, A60 (2020).
388. F. Stahler, S. W. Palla, in *The Formation of Stars* (Wiley-VCH Verlag GmbG & Co, 2004).
389. S. Stanimirovic, in *Single-Dish Radio Astronomy: Techniques and Applications* (Stanimirovic, Snezana et al., 2002), vol. 278, pp. 375–396.
390. T. P. Stecher, D. A. Williams, *Astrophys. Lett.* **4**, 99 (1969).
391. D. P. Stevenson, D. O. Schissler, *J. Chem. Phys.* **29**, 282 (1958).
392. S. E. Strom, G. L. Grasdalen, K. M. Strom, *ApJ* **191**, 111–142 (1974).
393. K. Sugitani, Y. Fukui, K. Ogura, *ApJS* **77**, 59 (1991).
394. A. N. Suutarinen *et al.*, *MNRAS* **440**, 1844–1855 (2014).

395. A. Suutarinen, http://oro.open.ac.uk/61309/, PhD thesis, Dept. of Physics, The Open University, 2015.
396. A. Suutarinen, *omnifit v0.1*, https://doi.org/10.5281/zenodo.29354, 2015.
397. K. N. R. Taylor, J. W. V. Storey, *MNRAS* **209**, 5P–10 (1984).
398. S. Terebey, F. H. Shu, P. Cassen, *ApJ* **286**, 529–551 (1984).
399. J. Terwisscha van Scheltinga *et al.*, *A&A* **611**, A35 (2018).
400. W.-F. Thi *et al.*, *A&A* **449**, 251–265 (2006).
401. A. G. G. M. Tielens, W. Hagen, *A&A* **114**, 245–260 (1982).
402. J. J. Tobin *et al.*, *Nature* **492**, 83–85 (2012).
403. J. J. Tobin *et al.*, *ApJ* **805**, 125 (2015).
404. W. Tscharnuter, *A&A* **39**, 207 (1975).
405. B. E. Turner, *ApJ* **501**, 731–748 (1998).
406. Ł. Tychoniec *et al.*, *A&A* **632**, A101 (2019).
407. Ł. Tychoniec *et al.*, *A&A* **640**, A19 (2020).
408. M. Vasta *et al.*, *A&A* **537**, A98 (2012).
409. A. I. Vasyunin, E. Herbst, *ApJ* **769**, 34 (2013).
410. A. I. Vasyunin *et al.*, *ApJ* **842**, 33 (2017).
411. F. Vazart *et al.*, *MNRAS* **499**, 5547–5561 (2020).
412. R. Visser, S. D. Doty, E. F. van Dishoeck, *A&A* **534**, A132 (2011).
413. R. Visser *et al.*, *A&A* **495**, 881–897 (2009).
414. S. N. Vogel *et al.*, *ApJ* **283**, 655–667 (1984).
415. C. M. Wade, *AJ* **62**, 148 (1957).
416. A. F. Wagner, M. M. Graff, *ApJ* **317**, 423 (1987).
417. V. Wakelam *et al.*, *Molecular Astrophysics* **9**, 1–36 (2017).
418. C. Walsh *et al.*, *ApJ* **823**, L10 (2016).
419. F. M. Walter *et al.*, *Mem. Soc. Astron. Italiana* **68**, 1081–1088 (1997).
420. H. Wang *et al.*, *ApJ* **617**, 1191–1203 (2004).
421. N. Watanabe, A. Kouchi, *ApJ* **571**, L173–L176 (2002).
422. Y. Watanabe *et al.*, *ApJ* **745**, 126 (2012).
423. W. D. Watson, E. E. Salpeter, *ApJ* **174**, 321 (1972).
424. W. D. Watson, *ApJ* **183**, L17 (1973).
425. J. C. Weingartner, B. T. Draine, *ApJ* **548**, 296–309 (2001).
426. A. Weiß *et al.*, *A&A* **365**, 571–587 (2001).
427. M. S. Westley *et al.*, *Nature* **373**, 405–407 (1995).
428. G. J. White, M. M. Casali, C. Eiroa, *A&A* **298**, 594 (1995).
429. B. A. Whitney *et al.*, *ApJ* **598**, 1079–1099 (2003).
430. D. C. B. Whittet *et al.*, *ApJ* **742**, 28 (2011).
431. D. A. Williams, S. Viti, *Observational Molecular Astronomy: Exploring the Universe Using Molecular Line Emissions* (Cambridge University Press, 2013).
432. J. P. Williams, W. M. J. Best, *ApJ* **788**, 59 (2014).
433. J. P. Williams, L. A. Cieza, *ARA&A* **49**, 67–117 (2011).
434. T. L. Wilson, *Reports on Progress in Physics* **62**, 143–185 (1999).
435. T. L. Wilson, F. Matteucci, *A&A Rev.* **4**, 1–33 (1992).
436. A. J. Winter *et al.*, *MNRAS* **491**, 903–922 (2020).
437. M. G. Wolfire, D. Hollenbach, A. G. G. M. Tielens, *ApJ* **344**, 770 (1989).
438. E. L. Wright *et al.*, *AJ* **140**, 1868–1881 (2010).

439. B. Yang *et al.*, *ApJ* **718**, 1062–1069 (2010).
440. H.-W. Yi *et al.*, *ApJS* **236**, 51 (2018).
441. H.-W. Yi *et al.*, *arXiv e-prints*, arXiv:2103.03499 (2021).
442. L. Zamirri *et al.*, *MNRAS* **480**, 1427–1444 (2018).
443. G. Zasowski *et al.*, *ApJ* **694**, 459–478 (2009).
444. F. Zernike, *Physica* **5**, 785–795 (1938).
445. C. Y. Zhang *et al.*, *A&A* **218**, 231–240 (1989).
446. C. Zhang *et al.*, *MNRAS* **497**, 793–808 (2020).
447. Z.-Y. Zhang *et al.*, *Nature* **558**, 260–263 (2018).
448. C. Zucker *et al.*, *ApJ* **879**, 125 (2019).
449. C. Zucker *et al.*, *A&A* **633**, A51 (2020).
450. P. H. van Cittert, *Physica* **1**, 201–210 (1934).
451. E. F. van Dishoeck, in *Millimetre and Submillimetre Astronomy* (Wolstencroft, R. D. and Burton, W. B., 1988), vol. 147, p. 117.
452. E. F. van Dishoeck, J. H. Black, *ApJS* **62**, 109 (1986).
453. E. F. van Dishoeck, E. A. Bergin, *arXiv e-prints* (2020).
454. E. F. van Dishoeck, J. H. Black, *ApJ* **334**, 771 (1988).
455. E. F. van Dishoeck, G. A. Blake, *ARA&A* **36**, 317–368 (1998).
456. M. L. van Gelder *et al.*, *A&A* **639**, A87 (2020).
457. S. E. van Terwisga *et al.*, *A&A* **640**, A27 (2020).
458. H. C. van de Hulst, *Recherches Astronomiques de l'Observatoire d'Utrecht* **11**, 2.i–2 (1946).
459. M. L. R. van 't Hoff *et al.*, *A&A* **599**, A101 (2017).
460. M. L. R. van 't Hoff *et al.*, *ApJ* **864**, L23 (2018).